Quantum Inspired Super-resolution

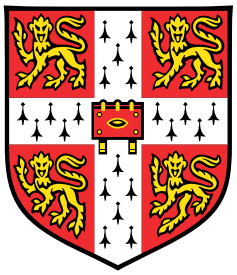

Candidate 8264V

Supervisor: Dr. David Arvidsson-Shukur

Department of Physics, Cavendish
University of Cambridge

This dissertation is submitted for the degree of
Master of Science

Peterhouse February 2025

Declaration

I hereby declare that except where specific reference is made to the work of others, the contents of this dissertation are original and have not been submitted in whole or in part for consideration for any other degree or qualification in this, or any other university. This dissertation is my own work and contains nothing which is the outcome of work done in collaboration with others, except as specified in the text and Acknowledgements. This dissertation contains fewer than 5,000 words over all the sections excluding abstract, appendices, bibliography, footnotes, tables and equations and has fewer than 30 pages for the main body.

Candidate 8264V
February 2025

Abstract

Traditional imaging methods for closely spaced photon sources typically depend on detecting their spatial intensity distribution. However, when the distance between these sources decreases beyond a certain threshold, the information regarding their separation diminishes, a phenomenon commonly known as "Rayleigh's curse," governed by Rayleigh's limit.

This study primarily aims to develop a quantum super-resolution algorithm with the following objectives: (i) overcoming the curse to precisely estimate the separation of incoherent sources from a far field in the "sub-Rayleigh" regime, where conventional methods struggle to differentiate two separate sources from a single light source due to extensive overlap, and (ii) utilizing the interference pattern of photons reflected from two closely spaced objects to explore their "sub-Rayleigh" features. The second task, owing to the coherent nature of the interfering wavefronts, is termed "coherent estimation," while the first one is referred to as "incoherent estimation." Specifically, quantum resources are employed in the parameter estimation process to minimize errors beyond the reach of conventional methods.

In the realm of incoherent source separation estimation, my approach provides partial immunity against Rayleigh's curse, resulting in a quadratic enhancement in estimation precision. Additionally, in coherent estimation, the study demonstrates quadratic improvements in precision scaling for sub-Rayleigh parameter estimation based on Quantum Fisher Information, which sets an upper limit on estimation precision. To summarise, my results leverage quantum phenomena to quadratically improve light detection in coherent and incoherent settings.

Table of contents

Chapter 1

Background

1.1 Introduction

In 1879, Lord Rayleigh introduced a criterion for evaluating the resolution of incoherent imaging based on the separation of two distant photon sources. If these sources are positioned closer than the width of their point spread function (which represents the response of the optical imaging system to a point source), their detected images overlap significantly, making them indistinguishable, as demonstrated in Fig 1.1. Therefore, resolution can be quantified by how accurately one can estimate the separation between two point sources, with photon shot noise being the most fundamental source of intensity measurement errors. By meticulously measuring the intensity profile, resolution can be enhanced using statistical inference theory.

Helstrom [1] pioneered the statistical theory in 1969 and formulated the theory of quantum detection and estimation, believing that quantum mechanics governs the fundamental limit of resolution due to the quantum nature of light. He subsequently studied the problem of locating an incoherent point source from far-field measurements as shown in Fig 1.2. Although he showed that the quantum limit is close to the ideal performance of direct imaging [2], which measures the intensity on the image plane, he did not propose an experimental setup.

Decades later, advancement by Tsang et al. [4] revealed a surprising insight: it is possible to resolve two incoherent point sources by applying quantum estimation theory to outcomes of far-field measurements. The efficacy of their methods, spatial-mode demultiplexing (SPADE)[1] as shown in Fig 1.3, has also been confirmed experimentally [5].

Their work demonstrated that measuring the photons from distant sources in a judicious basis of spatial modes can approach the quantum limits and offer substantial improvements. The quantum perspective has since inspired many follow-up studies and grown into a field of

[1] In this thesis, highlighted places are essential concepts to which the reader should pay extra attention or the main results I have derived.

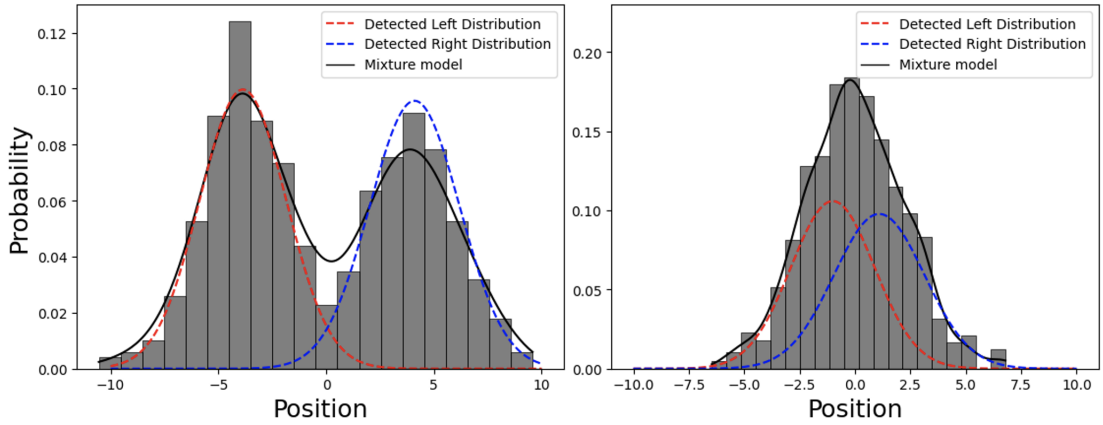

Fig. 1.1 I simulate possible intensity distributions detected at the image plane in the grey histogram. These distributions are modelled with Gaussian point spread functions (red and blue) representing two photon sources (left and right). We employ Maximum Likelihood Estimation (black line) for the Gaussian mixture model to illustrate the capability to resolve these sources. Double the Rayleigh Limit separates the sources in the left plot. Here, we observe two distinguishable peaks in the intensity distribution. On the top right, the sources are separated by less than one Rayleigh limit, so we can no longer discern two peaks in the intensity distribution.

research called quantum-inspired superresolution, potentially benefiting many applications in astronomy as well as fluorescence microscopy. One of the most promising uses of superresolution is range resolution, which is the ability to determine the distance between two objects along the same line of sight when performing remote sensing. Jordan et al. [7] dubbed it "super radar" and applied single parameter estimation to determine the spatial difference between two closely positioned objects. Owing to the coherent nature of the interfering wavefronts, I term it "coherent estimation". The pulses reflected from the two objects at slightly different positions, as depicted in Fig 1.4, are analogous to the far-field sources considered by Tsang. With quantum estimation theory, Jordan overcame the spatial Rayleigh resolution limit and demonstrated several orders of magnitude improvements in range resolution beyond known limits. This resolution improvement is essential for military applications and has significant potential for probing minute objects such as silicon chips in the semiconductor industry.

This thesis focuses on improving both Jordan's "super radar" technique as well as Tsang's incoherent source separation estimation:

- The range resolution primarily concerns the challenge of estimating a single parameter, the position difference between two objects. In the original paper [6], the authors considered the interference of two pulses reflected from the two closely separated

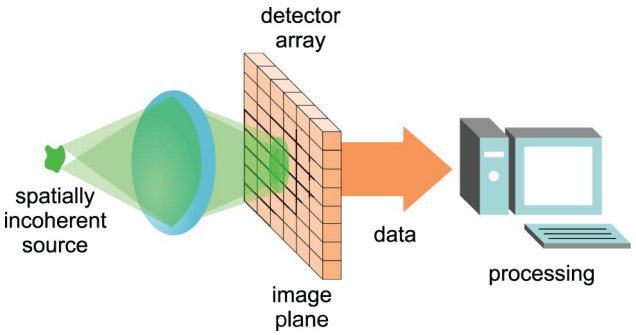

Fig. 1.2 Schematic diagram for direct imaging method. A distant source is focused on the image plane, and data is collected to reconstruct the parameter of interest. Image adapted from [3].

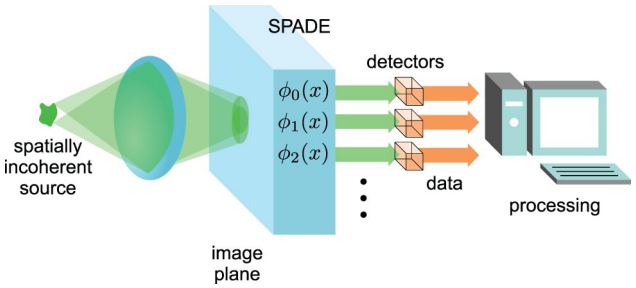

Fig. 1.3 Schematic diagram for SPADE. The distant source is decomposed into the different spatial mode ϕ_n based on its point spread function. A photon counter subsequently detects each mode, and the measurement results are processed with statistical theory. Image adapted from [3].

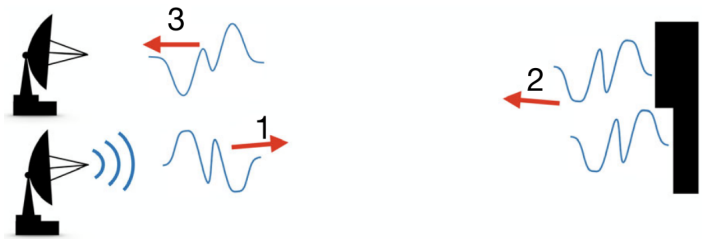

Fig. 1.4 Schematic diagram for "super radar". A pulse (photon) is sent through and reflected from the walls. The small distance difference l on the right is then estimated based on the interference information. Conventionally, if $l \leq c\tau/2$, where c represents the speed of light and τ denotes the pulse width, then the small separation could not be resolved easily, which is the equivalent of Rayleigh's curse in the incoherent source scenario. Image adapted from [6].

objects with equal intensity. They also assumed that the exact position of the centre of the two objects is known. However, this is not always the case, as the roughness of the detected objects commonly causes energy loss of the incoming photon, thus altering the intensity ratio compared to the original pulse. Moreover, it is hard to locate the position, which I call the "centroid," where the reflections happen with certainty. By relaxing these assumptions, this thesis delves into quantifying multi-parameter estimation involving the separation, centroid, and intensity ratio. I demonstrate a quadratic enhancement in quantum resolution compared to conventional imaging methods. Additionally, I briefly explain why a single photon source is the necessary experimental component for my theoretical findings.

- The reason to revisit Tsang's work is that recent results showed that the quantum advantage of SPADE vanishes in the presence of dark counts [8] or measurement crosstalk [9] between different spatial modes. Meanwhile, the presence of thermal background noise [10] questions the experimental feasibility of the estimation process on two incoherent thermal point sources. Alternative quantum methods, such as Quantum State Discrimination, largely mitigate these challenges. I draw inspiration from prior research [11] and utilize the quantum framework to yield the essential quantum advantage over classical imaging. I achieved a quadratic improvement in the weak secondary source limit. That is to say, the intensity contrast between the sources is high in my toy model. As is often the case in astronomical problems like exoplanet search, the contrast between stars and their orbiting planets varies immensely, ranging from $10^5 : 1$ for hot gas giants resembling Jupiter to an astonishing $10^{10} : 1$ for cooler Earth-like worlds [12]. This model creates a considerable hurdle for SPADE both experimentally and theoretically as the noise from photons arriving from the star overwhelms the faint signal emitted by the exoplanet.

1.2 Background

In this section, I will outline the background necessary for grasping the subjects addressed in this thesis. Initially, I provide a succinct overview of some critical concepts in quantum mechanics and relate them to classical direct imaging. Subsequently, I will delve into the fundamental theory behind quantum metrology, the quantum counterpart of parameter estimation. Finally, the last section will focus on elucidating the formulation of hypothesis decision theory in Quantum State Discrimination.

1.2.1 Quantum Formalism

Quantum mechanics, in principle, is a statistical theory with probability distributions. The probability density associated with a quantum state is called the density matrix, defined as the outer product of the state with its conjugate transpose:

$$\hat{\rho}_{\text{pure}} = |\Psi\rangle\langle\Psi| . \tag{1.1}$$

This matrix must be positive semi-definite, Hermitian, and of trace one. However, not all density matrices can be fully described with one state (pure states); a convex combination of density matrices is required to fully describe a system (mixed states):

$$\hat{\rho}_{\text{mix}} = \sum_i p_i \hat{\rho}_i, \quad \sum_i p_i = 1. \tag{1.2}$$

From the axioms of quantum mechanics, a measurement is given by a Positive Operator Valued Measure (POVM)—a collection of positive semi-definite operators, $\hat{M} = \{\hat{M}_1, \hat{M}_2, ..., \hat{M}_n\}$, that sum to the identity operator over the Hilbert space, $\sum_{i=1}^{n} \hat{M}_i = \hat{1}$. According to the Born rule, the probability outcome of one projective measurement $\hat{M}_m$ will given outcome m with probability:

$$\Pr(\mathrm{m}, \hat{\rho}) = \mathrm{Tr}[\hat{\rho}\hat{\mathrm{M}}_{\mathrm{m}}]. \tag{1.3}$$

Suppose we wish to take an intensity measurement of two distant incoherent sources. Following [13], we take the time window for detection sufficiently small that at most one photon is detected at a time:

$$\hat{\rho} = (1-\delta)\,|\text{vac}\rangle\langle\text{vac}| + \delta\hat{\rho}_1 + \mathscr{O}(\delta^2). \tag{1.4}$$

The coefficient $\delta << 1$ is the average photon number per temporal mode. It is clear that most of the photons are not collected, being in the $|\text{vac}\rangle\langle\text{vac}|$ vacuum state. The part we are interested in is $\hat{\rho}_1$, the single-photon density operator. I should stress that a subtlety lies in the difference between an Object Space state and an Image Space state [14], but I will not address it here, and for the rest of the thesis, we can consider them as the same thing. For incoherent scenes imaged in 1-dimension, the single-photon density takes the form:

$$\hat{\rho}_1 = \int_{-\infty}^{\infty} dx\, |\Psi_x\rangle\langle\Psi_x| , \quad |\Psi_x\rangle = \int_{-\infty}^{\infty} dx'\, \psi(x'-x)\, |x'\rangle . \tag{1.5}$$

Physically, $\psi(x)$ is the point spread function of the imaging system, and $|x'\rangle = \hat{a}^{\dagger}(x')\,|\text{vac}\rangle$ is a 1-photon excitation of the Dirac delta mode $\delta(x'-x)$ at the location x in the image plane.

Throughout the thesis, I assume a Gaussian normalized point spread function:

$$\psi(x) = \frac{1}{(2\pi\sigma^2)^{1/4}} e^{-\frac{x^2}{4\sigma^2}}. \tag{1.6}$$

Normalization condition is imposed with $\int_{-\infty}^{\infty} \psi^*(x)\psi(x)dx = 1$ and σ characterize the width of the function, associated with the Rayleigh's resolution limit. A distance smaller than the limit is termed "sub-Rayleigh."

In classical direct detection, the intensity distribution is measured in the position basis, $\text{POVM}_{\text{DD}} = \{\hat{\Pi}_{\text{x}} = |\text{x}\rangle\langle\text{x}|\}$. For instance, if we were to measure photons generated by two incoherent sources with an equal probability, $\hat{\rho}_1 = \frac{1}{2}(|\Psi_{\text{left}}\rangle\langle\Psi_{\text{left}}| + |\Psi_{\text{right}}\rangle\langle\Psi_{\text{right}}|)$, then the probability distribution of position space will yield:

$$\Pr(|\text{x}\rangle\langle\text{x}|, \hat{\rho}_1) = \text{Tr}[\hat{\rho}_1 |\text{x}\rangle\langle\text{x}|] \tag{1.7}$$

$$= \frac{1}{2}(|\langle x|\Psi_{\text{left}}\rangle|^2 + |\langle x|\Psi_{\text{right}}\rangle|^2). \tag{1.8}$$

Furthermore, $|\Psi_{\text{left}}\rangle$, $|\Psi_{\text{right}}\rangle$ are the single-photon pure states for photons emitted by the left and right source in the field respectively.

1.2.2 Quantum Metrology

The primary objective of quantum metrology is to achieve the highest possible accuracy in estimating unknown parameters. By harnessing quantum resources as probes, achieving a level of measurement precision that surpasses what can be attained through classical strategies becomes feasible. Quantum parameter estimation constitutes a cornerstone of metrology, and this section explains its general theory. I will introduce the pivotal theoretical tool within this framework—Quantum Fisher Information.

Statisticians focus on efficiently inferring hidden parameters from a probabilistic dataset. Quantum metrology is the quantum counterpart of the classical parameter estimation process. Typically, a comprehensive quantum-metrological procedure comprises four stages: (1) preparing the probe state; (2) parameterizing; (3) measuring; and (4) classical estimation, as shown in Fig 1.5 [15].

Suppose an experimental realization gives a N-point data set $\boldsymbol{x} = \{x_1, x_2, ..., x_N\}$, corresponding to the number of times the experiment is repeated. Each output $x_i, i = 1, ..., N$ is a random variable independently and identically distributed according to the same probability

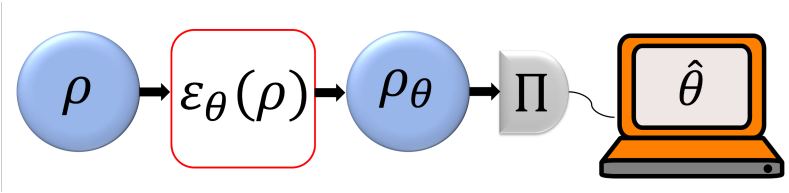

Fig. 1.5 Generalized steps in quantum metrology. A state ρ is prepared and parameterized with an unknown variable θ. A POVM operation Π is subsequently performed. The last step, the classical estimation, is well-studied in the literature of classical statistics. The first three steps are called quantum parameter estimation overall.

distribution, $p(\boldsymbol{x}|\boldsymbol{\theta})$[2], conditioned on the unknown parameter $\boldsymbol{\theta}$. Then, the estimator, $\hat{\boldsymbol{\theta}}$, is the method selected to obtain an estimate of $\boldsymbol{\theta}$. The estimator is precise if the probability distribution has a small variance around its mean value:

$$\mathrm{Var}(\hat{\boldsymbol{\theta}}) = \mathrm{E}[(\hat{\boldsymbol{\theta}} - \mathrm{E}[\hat{\boldsymbol{\theta}}]^2)]. \tag{1.9}$$

I will make an additional assumption throughout the thesis that our estimator is unbiased,

$$\mathrm{E}[(\hat{\boldsymbol{\theta}} - \boldsymbol{\theta})] = 0. \tag{1.10}$$

Helstrom formulated Fisher Information to explore the measured outcome's sensitivity to the unknown parameter. He sets a general lower bounds called Cramér-Rao bound on the parameter estimation error; see Appendix A.2 for precise definitions. The simplest Cramér-Rao bound for single parameter estimation is given as

$$\mathrm{Var}(\hat{\theta}) \geq \frac{1}{\mathrm{NF}(\theta)}, \tag{1.11}$$

where $\mathrm{F}(\theta)$ is the Fisher Information, with N being the number of experiments performed. In this thesis, we are more interested in multi-parameter estimation, and the multivariate Cramér-Rao bound is:

$$\mathrm{Cov}(\hat{\boldsymbol{\theta}}) \geq \frac{\mathscr{F}^{-1}(\boldsymbol{\theta})}{\mathrm{N}}. \tag{1.12}$$

Here, instead of variance, we have covariance as the error measure, and the inverse of Fisher Information now becomes the inverse of Fisher Information Matrix $\mathscr{F}(\boldsymbol{\theta})$. It is worth noting that the error can reach the Cramér-Rao bound in many situations, including an asymptotic limit where the sample size approaches infinity.

[2]Note here the bold symbol is a representation of a multi-parameter variable instead of a single-parameter variable.

The Quantum Fisher Information is the quantum analogue of the (classical) Fisher Information, which characterizes the sensibility of a parameterized quantum state to parameter changes. To this point, all theories define the bound on precision estimation for a given measurement strategy (a given POVM). In quantum mechanics, however, we have infinite choices of the measurement basis, and to maximize the Fisher Information, we need to find the optimal strategy:

$$\mathscr{Q}(\rho(\boldsymbol{\theta})) = \max_{\{\hat{\Pi}_{\boldsymbol{x}}\}} \mathscr{F}(p(\boldsymbol{x}|\rho(\boldsymbol{\theta}))). \tag{1.13}$$

The probability distribution $p(\boldsymbol{x}|\rho(\boldsymbol{\theta}))$ is naturally obtained from the POVM measure, $p(\boldsymbol{x}|\rho(\boldsymbol{\theta})) = \mathrm{Tr}[\rho(\boldsymbol{\theta})\hat{\Pi}_{\boldsymbol{x}}]$, and again I consider the Quantum Fisher Information Matrix $\mathscr{Q}(\rho(\boldsymbol{\theta}))$ for the multi-parameter estimation. The multivariate Quantum Cramér-Rao bound is given as,

$$\mathrm{Cov}(\hat{\boldsymbol{\theta}}) \geq \frac{\mathscr{F}^{-1}(\boldsymbol{\theta})}{\mathrm{N}} \geq \frac{\mathscr{Q}^{-1}(\boldsymbol{\theta})}{\mathrm{N}}. \tag{1.14}$$

The bound defines fundamentally the lowest error allowed by the laws of physics for any unbiased estimator. For any choice of quantum measurement that one may apply (any POVM), the Quantum Cramér-Rao bound establishes the minimum achievable uncertainty on an unbiased parameter estimate. The second inequality results from the fact that measurements can not extract more information than the quantum state. Nevertheless, we should note that the optimal POVM is sometimes hard to calculate and perform experimentally. More details are included in Appendix A.

The quantum advantage becomes clearer when illustrated with an example. I adopt the spatial mode measurement proposed by Tsang [4] as the quantum method to estimate the separation between two incoherent sources. I follow the convention of using the position basis as the POVM for classical direct imaging. To compare the estimate's precision, which is the source separation, we need to characterize the variance with Fisher Information. The specifics of Fisher Information depend on the point spread function, which we assume here to be Gaussian. However, the general behaviour follows: The Fisher Information remains relatively constant if the sources are well separated relative to Rayleigh's criterion. However, when the separation is close to Rayleigh's criterion or begins to violate it (smaller than the Rayleigh limit), the available information decays to zero, leading to the variance ballooning. However, when measured in the spatial mode, explicitly using the Hermite-Gauss basis for a Gaussian point spread function, the Quantum Fisher Information remains constant and unified upon normalization. This results in a constant variance, as depicted in Fig 1.6. However, I should inform the readers that the Hermite-Gauss mode conversion is similar to the Fourier transformation and hard to implement experimentally. The detailed calculation is provided in Appendix A.3.

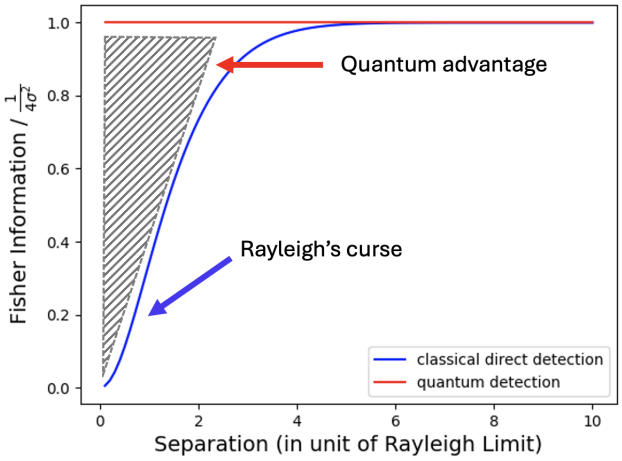

Fig. 1.6 A visualization of the Fisher Information of both direct detection (classical) and imaging in the Hermite-Gauss (HG) model basis (the optimal basis). I assume a Gaussian normalized point spread function with σ (Rayleigh's limit). Variance is lower bounded by the inverse of Fisher Information; thus, when the separation is small, the variance diverges for direct imaging. The separation (x-axis) is expressed in the unit of Rayleigh's limit. The Fisher Information on the y-axis is in the scale of the Fisher Information for the quantum method as shown in A.3. The grey dashed lines are regions of the quantum advantage indicated by the red arrow. The purple arrow indicates where Rayleigh's curse occurs when the separation is small.

1.2.3 Hypothesis Testing

In Section 1.1, I outlined the shortcomings of the SPADE method. An alternative approach lies in hypothesis testing, a sub-branch of Quantum State Discrimination. Hypothesis testing preserves the quantum advantage over classical strategies and offers ease of experimental implementation while circumventing the challenges encountered with SPADE. This section will explain how the parameter estimation problem simplifies into a hypothesis test and seamlessly incorporates the incoherent estimation with quantum hypothesis testing.

Hypothesis testing entails making a binary decision between two exclusive possibilities: H_0 (the null Hypothesis) and H_1 (the alternative Hypothesis). For example, in [11], the authors considered two incoherent sources, the binary system of a bright star and a dim planet, as a toy model. In this star-exoplanet model, they tried to determine whether there is (H_1) or is not (H_0) a planet orbiting a distant star as depicted in Fig 1.7 based on collected data. Due to limited data, this decision is prone to errors. Given the rarity of exoplanets, the aim is to minimize the risk of false negatives (type-II errors, β) while being somewhat tolerant of false positives (type-I errors, α) as long as they remain below a specified threshold

Table 1.1 Summary of scenarios that could happen in the described hypothesis test and the associated event probability.

	H_0, no planet	H_1, with planet
Reject H_0	Type-I error, False positive α	correct decision $1-\beta$
Accept H_0	correct decision $1-\alpha$	Type-II error, False negative β

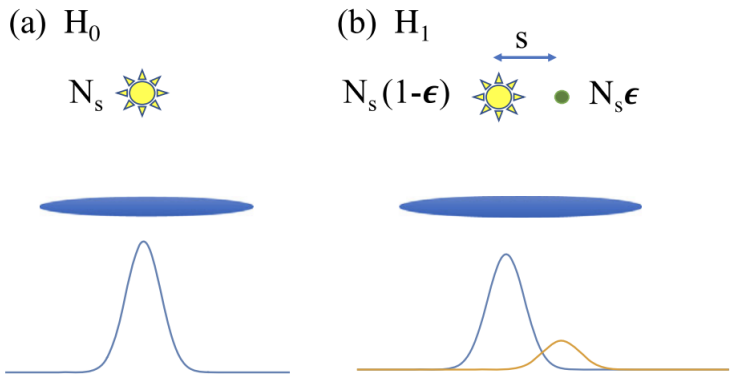

Fig. 1.7 Hypothesis H_0 is that only one source (a), the star, is present of intensity N_s. Hypothesis H_1 is that both sources are present (b), with total intensity N_s and relative intensity $\varepsilon/(1-\varepsilon) \ll 1$. The two sources are separated by s.

to prevent excessive data analysis. The potential hypothesis outcomes are summarized in Table 1.1.

Suppose one measure N identical copies of an unknown single-photon field state (either ρ_0 or ρ_1) and the type-I error is restricted to $\alpha_N \in (0,\gamma)$, with $\gamma < 1$ so as not to cause too much trouble with false positives. The minimum probability of error for discriminating whether the field state is ρ_0 or ρ_1 asymptotically follows the Quantum Stein's Lemma [16] with large N [16, 17],

$$\beta_N \sim \exp[-ND(\rho_0||\rho_1)] \tag{1.15}$$

$$\text{where} \quad \mathrm{D}(\rho_0\|\rho_1) = \mathrm{Tr}[\rho_0(\ln\rho_0 - \ln\rho_1)]. \tag{1.16}$$

Here, $D(\rho_0||\rho_1)$ is the Umegaki quantum relative entropy [18].

Finally, to demonstrate the quantum advantage over the classical method, we must define the classical counterpart of the type-II error bound. It simply involves replacing ρ_0 and ρ_1 with the classical probability distribution p_0 and p_1, the chances that H_0 and H_1 happen, respectively. The exponent in the bound thus becomes the classical relative entropy $D(p_0\|p_1)$. The trace operation consequently changes to an integration.

Chapter 2

Main Result

In this section, I will introduce two toy models for the incoherent and coherent estimations. I remind the reader that the ultimate goals of this thesis are: To precisely estimate the separation between two incoherent sources upon measuring the incoming photons, where the second source's intensity is comparably weaker, to assess the spatial characteristics between two closely positioned objects by analyzing the interference patterns generated by photons reflected from each object.

2.1 Incoherent Estimation

I will examine on the first problem with a simple Star-Exoplanet toy model. Photons are scattered by the star and planet in the binary system and subsequently detected on one's image plane. My scheme is much easier to implement than the SPADE method, which explicitly requires image inversion of the spatial modes. The quantum advantage remains during parameter estimation over the conventional approach.

2.1.1 Star-Exoplanet Model

We adopt an idealized approach, envisioning the star and the exoplanet as coherent quasi-monochromatic thermal point sources [19]. I disregard the sources' finite size and polychromatic emission spectra in this simplification. Additionally, I assume a static scene throughout the measurement period, disregarding the orbital dynamics of the planet around the star at the timescale of detection. Under these assumptions, the scene is fully characterized by the

parameters $\boldsymbol{\theta} = \{r_s, r_c, \varepsilon\}$,

$$r_{\text{star}} \equiv r_c + \frac{r_s}{2}, \tag{2.1a}$$

$$r_{\text{planet}} \equiv r_c - \frac{r_s}{2}, \tag{2.1b}$$

$$\varepsilon \in (0,1). \tag{2.1c}$$

Here, r_s and r_c are the separation and centre of the system when mapped to the focal plane, respectively. I define ε as the normalized brightness of the exoplanet: the star and the planet have ε and $1-\varepsilon$ as intensity coefficients, respectively, that sum to unity. Therefore, the toy model, assuming equal and unit variance, has the density matrix:

$$\rho = (1-\varepsilon)\left|\psi_{\text{star}}\right\rangle\!\left\langle\psi_{\text{star}}\right| + \varepsilon\left|\psi_{\text{planet}}\right\rangle\!\left\langle\psi_{\text{planet}}\right|, \tag{2.2}$$

$$\left|\psi_{\text{star}}(r_{\text{star}})\right\rangle = \int_{-\infty}^{\infty} dx \frac{1}{(2\pi)^{1/4}} e^{-\frac{(x-r_{\text{star}})^2}{4}} \left|x\right\rangle, \tag{2.3}$$

$$\left|\psi_{\text{planet}}(r_{\text{planet}})\right\rangle = \int_{-\infty}^{\infty} dx \frac{1}{(2\pi)^{1/4}} e^{-\frac{(x-r_{\text{planet}})^2}{4}} \left|x\right\rangle. \tag{2.4}$$

In this work, I will assume that the system's centre is at the origin of the transverse coordinate system, $r_c = 0$, which is reasonable as stated in [4]. I also focus on the 1-dimensional case only. In the meantime, we point the curious reader to [20] for an exciting discussion on how the interdependence of r_s, r_c, and ε manifests in the Fisher Information for the three-dimensional counterpart.

In conventional imaging, a converging optical system creates a focused image of an object on the image screen. The separation between the star and planet is thus approximated as the angular width $r \approx r_s/D$ where D is the distance to the emitter[1]. Moreover, the Rayleigh's limit, due to diffraction on the aperture of the imaging system, is $\text{Ry} = 1.22\lambda/R \sim \sigma$, where λ is the wavelength of the photon, R the size of the aperture and σ the characteristic width of the point spread function. When the angular width is comparable to or smaller than the Rayleigh length ($r << \sigma$), in the "sub-Rayleigh" region, direct imaging in a position basis no longer works for separation estimation. Although the SPADE method improved the resolution, a dim exoplanet in the proximity of a much brighter stellar source poses practical challenges to the quantum imaging measured in spatial modes. The alternative approach to avoid the experimental difficulty and demonstrate quantum advantage is the hypothesis testing described in Sec 1.2.3. However, unlike the previous hypothesis test, which is used for exoplanet "detection", I propose an exoplanet "localization" scheme with my Adaptive

[1]Without loss of generality, I will interchange the term angular width with separation here.

Table 2.1 Summary of scenarios that could happen in my proposed hypothesis test and the associated event probability.

	$H_0, r_{est} < r$	$H_1, r_{est} \geq r$
Reject H_0	Type-I error, False positive α	correct decision $1-\beta$
Accept H_0	correct decision $1-\alpha$	Type-II error, False negative β

Hypothesis Testing, as summarized in Algorithm 1. The main difference here is that the null hypothesis is now changed to a scenario where the star and the planet are separated by an estimated value r_{est}, which has to be smaller than the actual separation r. Different types of error are summarized in Table 2.1. My algorithm can effectively localize the position of the system instead of just detecting the presence of the weaker source. In other words, I am updating the measuring operators based on the data collected from the previous test, eventually leading to an optimal POVM for the measurement.

Algorithm 1: Adaptive Hypothesis Testing

Data: Set an empty array $\{r_{\text{est}}^{(1)}, r_{\text{est}}^{(2)}..r_{\text{est}}^{(N)}\}$ where N is the number of experiments and $r_{\text{est}}^{(\tau)}$ the estimated separation in each iteration.

Set up the Star-Exoplanet toy model with state $\rho(r)$;

Initialize guessed separation $r_{\text{est}}^{(1)} < r$;

Initialize worst-scenario POVM: $\hat{M}_{\text{est}}(r_{\text{est}}^{(1)}) = \{\hat{M}'_{\text{star}}, \hat{M}'_{\text{planet}}, \hat{M}'_{\text{Fail}}\}$;

Take measurements and obtain the probability distribution $P_{\text{star}}^{(1)} \leftarrow Tr[\rho(r)\hat{M}'_{\text{star}}]$;

$P_{\text{planet}}^{(1)} \leftarrow Tr[\rho(r)\hat{M}'_{\text{planet}}]$;

$n \leftarrow 1$;

while $n \leq N$ **do**

  hypothesis test with distribution $P_{\text{star}}^{(n)}$ and $P_{\text{planet}}^{(n)}$;

  construct $r^{\text{tmp}} = |r_{\text{star}} - r_{\text{planet}}|$ from the probability distributions;

  if Accept null hypothesis H_0 **then**

    $r_{\text{est}}^{(n+1)} \leftarrow r^{\text{tmp}}$;

    take measurement with $\hat{M}_{\text{est}}(r_{\text{est}}^{(n+1)})$;

    obtain the updated probability distribution $P_{\text{star}}^{(n+1)}$ and $P_{\text{planet}}^{(n+1)}$;

  else

    redo the experiment with a smaller r_{est}

  end

  $n \leftarrow n+1$;

end

To be certain of the locations of the star and the planet in the toy model, one needs to know from which source the collected photon is scattered. That is to say, one has to be conclusive in differentiating the state $|\psi(r_{\text{star}})\rangle$ from $\left|\psi(r_{\text{planet}})\right\rangle$. Discrimination is easy if the states are orthogonal: a projective measurement in the basis $\{|\psi(r_{\text{star}})\rangle\langle\psi(r_{\text{star}})|, \left|\psi(r_{\text{planet}})\right\rangle\left\langle\psi(r_{\text{planet}})\right|\}$ will determine the state with certainty. However, in the 'sub-Rayleigh' regime, the two states overlap, resulting in the non-orthogonality,

$$\begin{aligned} d = \left\langle\psi(r_{\text{star}})\middle|\psi(r_{\text{planet}})\right\rangle &= \int_{-\infty}^{\infty} dx \int_{-\infty}^{\infty} dx' \psi(x - r_{\text{star}}) \left\langle x\middle|x'\right\rangle \psi(x' - r_{\text{planet}}) \\ &= \int_{-\infty}^{\infty} dx \int_{-\infty}^{\infty} dx' \psi(x - r_c + \frac{r_s}{2}) \delta_{x,x'} \psi(x' - r_c - \frac{r_s}{2}) \\ &= \int_{-\infty}^{\infty} dx \psi(x - r_c + \frac{r_s}{2}) \psi(x - r_c - \frac{r_s}{2}) \\ &= e^{-r_s^2/8} = e^{-r^2 D^2/8} > 0. \end{aligned}$$

The best strategy now is to unambiguously discriminate the states at the cost of sometimes having an inconclusive result. This is achieved with the optimal POVM, $\hat{M}_{\text{opt}}(r) = \{\hat{M}_{\text{star}}, \hat{M}_{\text{planet}}, \hat{M}_{\text{Fail}}\}$. Without loss of generality, we express the original states as:

$$|\psi(r_{\text{star}})\rangle = \sqrt{1 - |d|^2} \left|\psi(r_{\text{planet}}^{\perp})\right\rangle + d \left|\psi(r_{\text{planet}})\right\rangle, \tag{2.5}$$

$$\left|\psi(r_{\text{planet}})\right\rangle = \sqrt{1 - |d|^2} \left|\psi(r_{\text{star}}^{\perp})\right\rangle + d \left|\psi(r_{\text{star}})\right\rangle, \tag{2.6}$$

$$\text{where} \quad \left\langle\psi(r_{\text{star}}^{\perp})\middle|\psi(r_{\text{star}})\right\rangle = 0, \left\langle\psi(r_{\text{planet}}^{\perp})\middle|\psi(r_{\text{planet}})\right\rangle = 0. \tag{2.7}$$

Then, the optimal POVM measure is chosen as:

$$\hat{M}_{\text{star}}(r_{\text{star}}) = \left|\psi(r_{\text{planet}}^{\perp})\right\rangle\left\langle\psi(r_{\text{planet}}^{\perp})\right|, \tag{2.8}$$

$$\hat{M}_{\text{planet}}(r_{\text{planet}}) = \left|\psi(r_{\text{star}}^{\perp})\right\rangle\left\langle\psi(r_{\text{star}}^{\perp})\right|, \tag{2.9}$$

$$\hat{M}_{\text{Fail}} = \hat{1} - \lambda_1 \hat{M}_{\text{star}} - \lambda_2 \hat{M}_{\text{planet}}, \tag{2.10}$$

with an appropriate choice of λ_1 and λ_2 depending on the intensity difference while satisfying that each element in the POVM is positive semi-definite.

For example, if a photon is detected with $\hat{M}_{\text{star}}$, then one is certain that the star scatters the photon because the probability of the other state goes to zero, as shown in Fig 2.1,

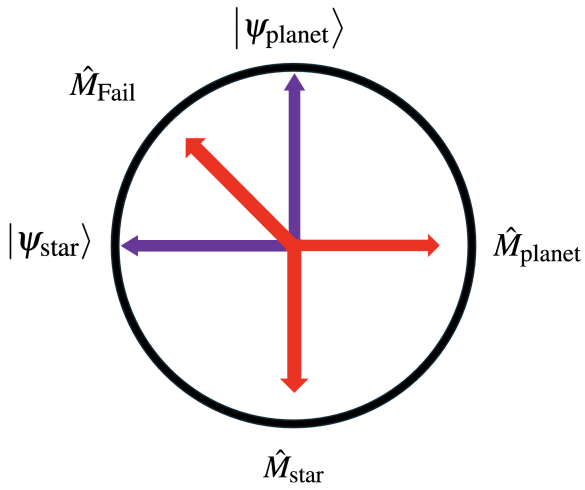

Fig. 2.1 Bloch sphere representation of states (in purple) and optimal POVM (in red) for unambiguous quantum state discrimination on the states $|\psi(r_{\text{star}})\rangle$ and $|\psi(r_{\text{planet}})\rangle$. The circle is a projection representation of the 3D Bloch sphere. Note that on the Bloch sphere, orthogonal states are antiparallel.

$$\text{Tr}[|\psi(\text{r}_{\text{planet}})\rangle\langle\psi(\text{r}_{\text{planet}})|\hat{\text{M}}_{\text{star}}] = 0, \tag{2.11}$$

$$\text{Tr}[|\psi(\text{r}_{\text{star}})\rangle\langle\psi(\text{r}_{\text{star}})|\hat{\text{M}}_{\text{planet}}] = 0. \tag{2.12}$$

However, without any prior knowledge of the system's position, the measurement is susceptible to errors, exemplified by $\text{Tr}[|\psi(\text{r}_{\text{planet}})\rangle\langle\psi(\text{r}_{\text{planet}})|\hat{\text{M}}'_{\text{star}}] \neq 0$. This discrepancy arises because the states $|\psi(r^{\text{est}\perp}_{\text{star}})\rangle$ and $|\psi(r^{\text{est}\perp}_{\text{planet}})\rangle$ may not be orthogonal to $|\psi(r_{\text{star}})\rangle$ and $|\psi(r_{\text{planet}})\rangle$, respectively. Hence, I will employ Adaptive Hypothesis Testing to mitigate this error.

The process begins with the implementation of the worst-case scenario POVM, denoted as $\hat{M}_{\text{est}} = \{\hat{M}'_{\text{star}}, \hat{M}'_{\text{planet}}, \hat{M}'_{\text{Fail}} = \hat{1} - \hat{M}'_{\text{star}} - \hat{M}'_{\text{planet}}\}$, based on the estimated separation r_{est}. Subsequently, I will utilize Maximum Likelihood Estimation, a widely accepted technique for estimating parameters within a presumed probability distribution, to analyze the observed data.

Following this, conducting a hypothesis test on the derived probability distributions will guide our decision to accept or reject the null hypothesis. If our estimated value falls short of the separation, we proceed to the next iteration with an updated POVM. Conversely, if the null hypothesis is invalidated, we adjust the initial estimation to an even smaller r_{est} to restart the process.

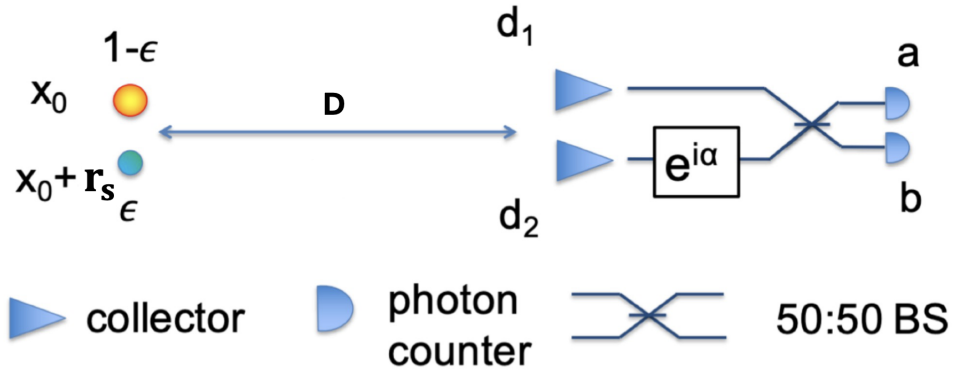

Fig. 2.2 Schematic of two sources with a separation of r_s, at a distance D from the collectors. Two collectors at d_1 and d_2 direct light into a two-mode interferometer consisting of a phase shift of α and a $50:50$ beam splitter, followed by photon counters a and b. This is the optical setup proposed by [21] to encode the parameters, the separation, and the intensity specifically, of the two incoherent sources in the object plane to the image plane with d_1, d_2, and α.

Thus, by continually updating the separation parameter adaptively, I aim to align $\hat{M}_{\text{est}}$ more closely with $\hat{M}_{\text{opt}}$ and bring r_{est} closer to the actual value r with each iteration.

Physically, the POVM in each run is implemented by measuring the photons using the setup illustrated in Fig 2.2. This optical conversion procedure combined with measurement in position basis is equivalent to applying $\hat{M}_{\text{est}}$ with a suitable choice of d_1, d_2 and α. This approach reduced the experimental complexity for large-baseline devices, while the SPADE method, suited for circular lenses and mirrors, is infeasible on a large scale.

Then after collecting the photons in the counter, one is supposed to reconstruct the POVM by adjusting the parameters in the optical setup based on the estimated state $\rho = (1-\varepsilon)\left|\psi^{\text{est}}_{\text{star}}\right\rangle\left\langle\psi^{\text{est}}_{\text{star}}\right| + \varepsilon\left|\psi^{\text{est}}_{\text{planet}}\right\rangle\left\langle\psi^{\text{est}}_{\text{planet}}\right|$. The positions, assuming the centre of the system lies at the origin, are $r^{\text{est}}_{\text{star}} = \frac{r^{\text{est}}}{2}$ and $r^{\text{est}}_{\text{planet}} = \frac{-r^{\text{est}}}{2}$ respectively. Meanwhile, the probability that the photon is detected at detectors a or b is used to conduct the hypothesis test.

2.1.2 Result

The Summary of the result is displayed in Table 2.3. There are a few things worth noticing:

- The Adaptive Hypothesis Testing effectively addresses the practical limitations inherent in the SPADE method.
- Within weak secondary source scenarios, the scaling (to be derived in this section) of the type-II error exhibits a quadratic enhancement in the exponent when transitioning

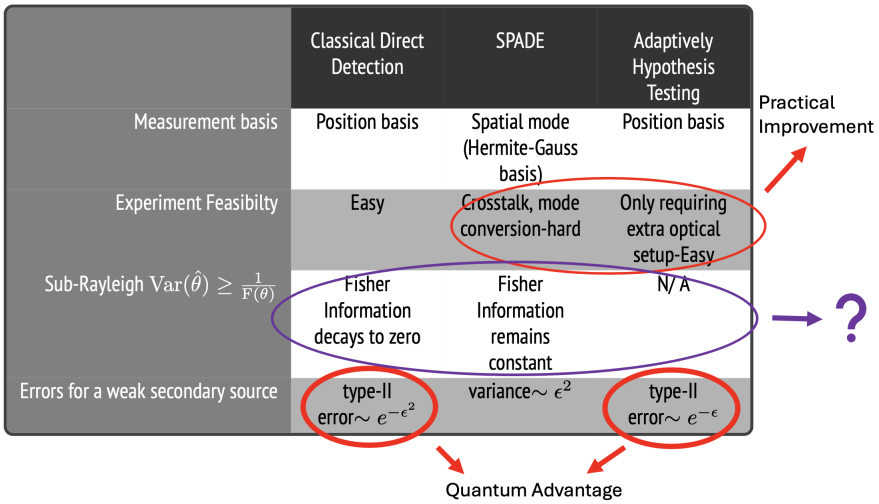

Fig. 2.3 Summary Table of Incoherent Estimation Results: The initial row presents three distinct methods analyzed in this thesis. Upon evaluating their experimental feasibility, the Adaptive Hypothesis Testing method exhibits an advantage over the SPADE method. As elaborated in the subsequent section, our proposed approach demonstrates superior type-II error scaling compared to classical methods in the weak secondary source limit. However, discerning the enhancement in the variance of our estimator, as denoted by the purple circle, may not be immediately apparent.

from the classical method to the quantum method. The boost bears a resemblance to Grover's algorithm [22], a renowned quantum search algorithm.

- However, as illustrated in Table 2.3, there is currently no discernible enhancement in the precision of my estimator for parameter estimation. This aspect warrants further numerical exploration, which I defer to future research endeavours.

In this toy model, envision an ideal experiment setup without any source of error. The only concern now is reducing the type-II error during our hypothesis test. Therefore, I will demonstrate how my quantum framework is inherently advantageous over the classical one.

The square of the Gaussian point spread function determines the intensity distribution on the image screen:

$$p_0(x) = (1-\varepsilon)|\psi_{\text{star}}(x-r_c)|^2 + \varepsilon|\psi_{\text{planet}}(x-r_c-r_{\text{est}})|^2. \tag{2.13}$$

By contrast, the actual intensity profile is[2]

$$p_1(x) = (1-\varepsilon)|\psi_{\text{star}}(x-r_c)|^2 + \varepsilon|\psi_{\text{planet}}(x-r_c-r)|^2, \tag{2.14}$$

[2]Here I will interchange the angular width r with the transverse distance r_s for simplicity.

where $\varepsilon << 1$, denoting the normalized intensity of light scattered by the exoplanet. With help of Eqn.(1.15), by requiring that the probability of a false positive, α_N, stays bounded away from 1, the probability β_N of a false negative classically scales like:

$$\lim_{N\to\infty}\frac{1}{N}\ln\beta_N = -D(p_0\|p_1), \quad \text{where} \quad \mathrm{D(p_0\|p_1)} = \int \mathrm{dx p_0(x)\left[\ln p_0(x) - \ln p_1(x)\right]}. \tag{2.15}$$

In Appendix B.2, I derived the following result:

$$D(p_0\|p_1) = (\frac{e^{r_{\text{est}}^2}+e^{r^2}}{2} - e^{r_{\text{est}}r})\varepsilon^2 + O\left(\varepsilon^3\right). \tag{2.16}$$

To reduce the error, we want to increase the relative entropy $D(p_0\|p_1)$. As the most prominent term in Eqn.(2.16) is quadratic in ε, r_{est} and r, this formally expresses the challenges of using direct detection when the separation is small.

Now quantum mechanically, the two hypotheses are associated with the density matrices[3]:

$$\rho_0 = (1-\varepsilon)\left|\psi_{\text{star}}(x-r_c)\right\rangle\left\langle\psi_{\text{star}}(x-r_c)\right| + \varepsilon\left|\psi_{\text{planet}}(x-r_c-r_{\text{est}})\right\rangle\left\langle\psi_{\text{planet}}(x-r_c-r_{\text{est}})\right|, \tag{2.17}$$

$$\rho_1 = (1-\varepsilon)\left|\psi_{\text{star}}(x-r_c)\right\rangle\left\langle\psi_{\text{star}}(x-r_c)\right| + \varepsilon\left|\psi_{\text{planet}}(x-r_c-r)\right\rangle\left\langle\psi_{\text{planet}}(x-r_c-r)\right|. \tag{2.18}$$

To calculate the quantum relative entropy, I need to find a basis set that spans the Hilbert space generated by $|\psi_{r_c}\rangle$, $|\psi_{r_c+r_{\text{est}}}\rangle$ and $|\psi_{r_c+r}\rangle$[4], using the Gram–Schmidt process:

$$|e_1\rangle = |\psi_{r_c}\rangle, \tag{2.19}$$

$$|e_2\rangle = \frac{|\psi_{r_c+r}\rangle - \omega_r|\psi_{r_c}\rangle}{\sqrt{1-\omega^2}}, \tag{2.20}$$

$$|e_3\rangle \sim |\psi_{r_c+r_{\text{est}}}\rangle - (\omega_e - \omega_r^2\omega_e - \omega_{re}\omega_r)|\psi_{r_c}\rangle - (\omega_{re} - \omega_r\omega_e)|\psi_{r_c+r}\rangle, \tag{2.21}$$

where $\omega_r = \langle\psi_{r_c}|\psi_{r_c+r}\rangle$, $\omega_e = \langle\psi_{r_c}|\psi_{r_c+r_{\text{est}}}\rangle$ and $\omega_{re} = \langle\psi_{r_c+r}|\psi_{r_c+r_{\text{est}}}\rangle$. Note $|e_3\rangle$ is correct up to a normalization factor.

Substituting this into Eqn.(1.15) with small ε expansion, I obtain the quantum relative entropy,

[3] Without loss of generality I can place the star at the origin of the coordinate system.

[4] For simplicity let us denote the positional dependence in the subscript.

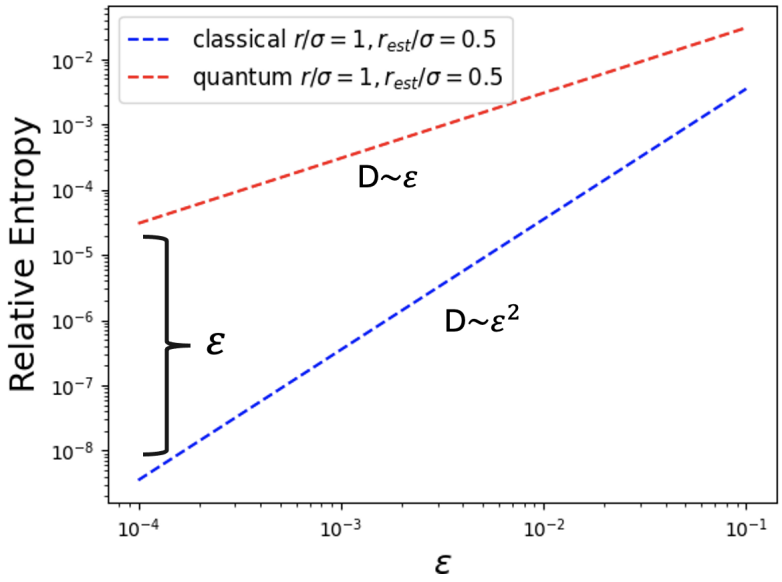

Fig. 2.4 Comparison between the quantum relative entropy (red) and the one for direct imaging (blue) based on the ε, for $r/\sigma = 0.1$ and the estimated value $r_{\text{est}}/\sigma = 0.5$. The log-log scale emphasizes the different scaling for small ε. The gap between the two dashed lines indicates the quantum advantage in reducing the type-II error of hypothesis testing.

$$D(\rho_0\|\rho_1) = \left(1 - \omega_r^2 + \frac{r^2 r_{est}^2 \left(r^2 - 4\log\left(\frac{1}{\omega_r^2} - 1\right)\right)}{64\left(\frac{1}{\omega_r^2} - 1\right)}\right)\varepsilon. \tag{2.22}$$

In Fig 2.4, the transition from ε^2 to ε highlights a significant gap between classical relative entropy and its quantum counterpart. This disparity underscores the advantage in relative entropy, demonstrating a substantial reduction in type-II errors through quantum estimation. This advantage is similarly illustrated in Fig 2.5. The likelihood of false negatives diminishes as r_{est} diverges from r, increasing entropy. Consequently, there is a higher probability of rejecting the current null hypothesis, indicating a narrower gap and subsequent adjustment of the estimated distance in subsequent iterations. This adjustment parallels separating sources for subsequent detection attempts, reducing overlap. Furthermore, the widening gap between quantum and classical estimations showcases improvements. Notably, the dip in the logarithmic plot may occur when the estimated value r_{est} closely approximates r. This suggests a tendency to accept the null hypothesis despite the smaller star-planet distance than my estimate. Nevertheless, this highlights the resilience of the quantum method against the hypothesis.

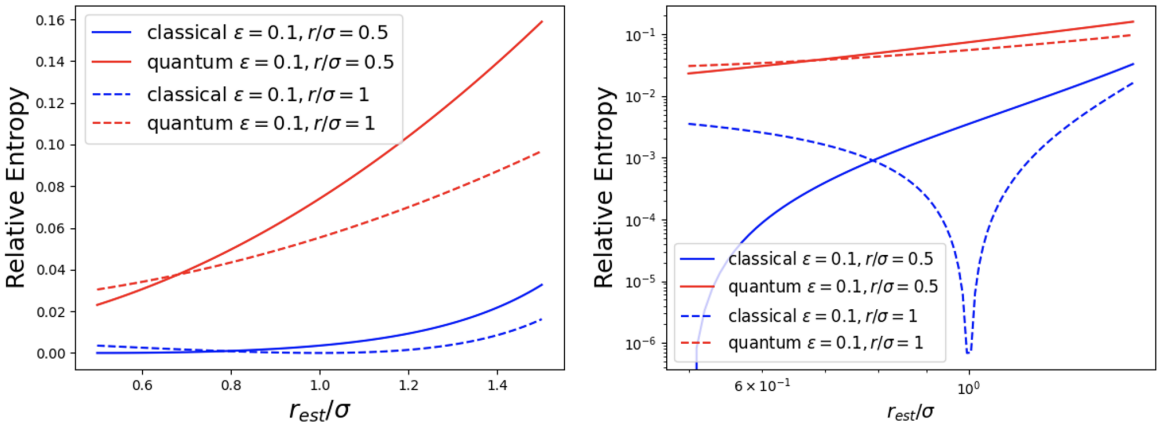

Fig. 2.5 Comparison between the quantum relative entropy and the one for direct imaging at $\varepsilon = 0.1$. Left figure: the entropies plotted vs r_{est}, for $r/\sigma = 0.5$ (solid line) and $r/\sigma = 1$ (dotted line). Right figure: Plots in the log-log scale. The dip and rapid drop in the classical entropy correspond to the fact that we are more likely to make false negative errors (entropy dropping to zero) because of the closeness of the estimated separation value and the actual one. The continual growth of quantum relative entropy illustrates its robustness. The gap between quantum relative entropy and classical one is narrower when the estimated value is smaller. This is not an issue because we only start with comparably large r_{est} in the right region with a large gap between the two relative entropies.

The quantum advantage is best illustrated with Fig 2.6 where the heat map is plotted with r as the x-axis and r_{est} as the y-axis. We can see clearly that when r is close to zero, almost no entropy is available to stabilize the classical hypothesis test. In contrast, the quantum counterpart with some entropy left keeps us from making type-II errors.

2.2 Coherent Estimation

In this section, I will introduce the quantum formulation of the coherent estimation problem. To effectively carry out the estimation process, we require a device capable of generating a photon pulse (a wavepacket) and subsequently transmitting this coherent pulse to the objects of interest, which are positioned at slightly varying locations. Therefore, I will first elucidate how a single photon source generates such a pulse in Section 2.2.1 and present the theoretical findings in Section 2.2.2.

2.2.1 Super Radar Model

Range resolution is vital in target characterization and imaging. One could utilize the interference pattern generated by photons reflected from each object to discern between

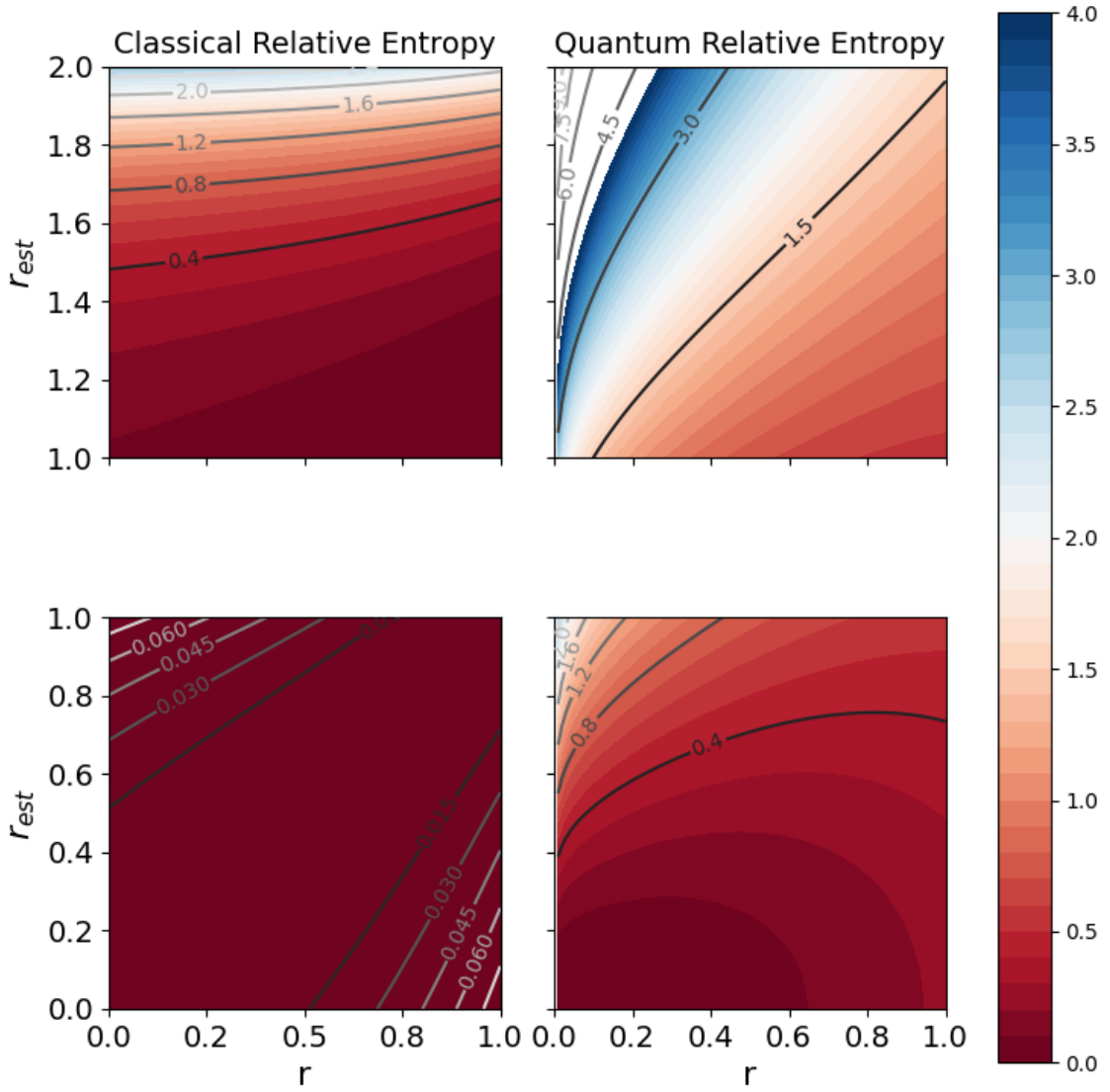

Fig. 2.6 Classical relative entropy (left column) and Quantum relative entropy (right column) plotted in heat map. The entropy is high in the white-blue region while low in the dark-red region. It is clear that when r is small, r_{est} has to be quite large for classical hypothesis testing to maintain finite relative entropy. While the curved contour line indicates r_{est} does not need to be far away from the true transverse distance to make the test accurate.

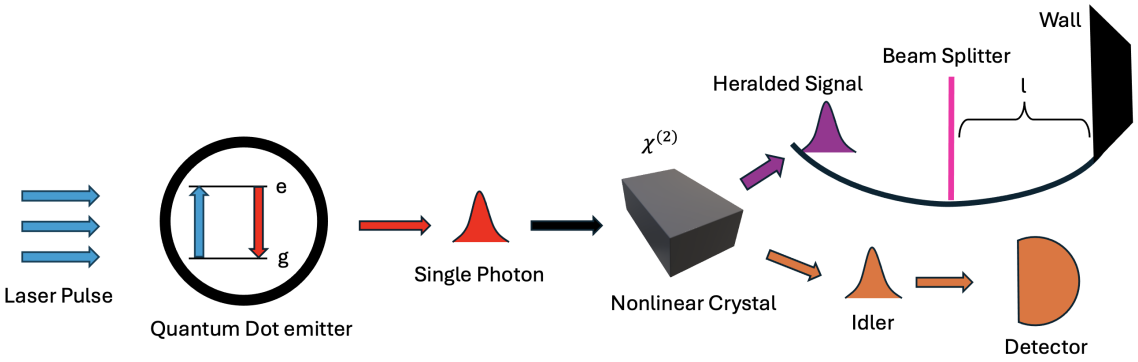

Fig. 2.7 Model for the "super radar" detection. The first few parts of the process, e.g. targeting the photon emitter with a laser beam, sending the single photon to the $\chi^{(2)}$ material, and creating a heralded photon, could be precisely done in experiment [24]. In the last step, the photon wavepacket hitting a beam splitter (pink) and interfering with the reflected pulses is an idealized situation in my toy model. I explicitly assume that the whole interference process takes place in a harmonic potential to stabilize the Gaussian wavepacket from spreading. The distance between the beam splitter and the wall is l, the range distance.

two objects at slightly different locations. Hence, a singular photon pulse is essential in the experimental setup. Consider shining a laser beam on a photon emitter like a semiconductor quantum dot. As the excited electrons in the quantum dot return to their lower energy states, they release energy as photons. By precise control of the quantum dot's properties, such as its size, shape, and composition, this process often results in the emission of a single photon. Then, the interaction with the nonlinear crystal, a $\chi^{(2)}$ material, will convert the high-energy photon into two lower-energy photons (signal and idler photons) that are entangled in various degrees of freedom, such as polarization. The heralded photon source holds particular significance in fields such as quantum key distribution [23], where entanglement ensures the security of the information exchange process. After confirming the available photon pulse, we send the photon to the two objects of interest, modelled as a beam splitter and a wall (as an infinite potential barrier), as shown in Fig 2.7. The coherent interference created from the pulse reflected from the wall and the pulse reflected from the beam splitter could greatly improve existing range resolution, as shown in Fig 2.8.

Following [25], let us suppose the distance between the beam splitter and the wall is l, and the splitting happens at l_0. Distinguishing the loss and sub-resolved detection pattern relies on the interference of scattering depths along the line of sight. I assume the character of the pulse shape is preserved by the intermediate medium, which will, in this thesis, be a Gaussian function $\psi(x)$. In reality, it will distort because of the frequency-dependency of the index of refraction. However, we must recognize the energy loss during evolution, resulting in different intensity coefficients. The resultant waveform in a unit of Rayleigh's limit σ is

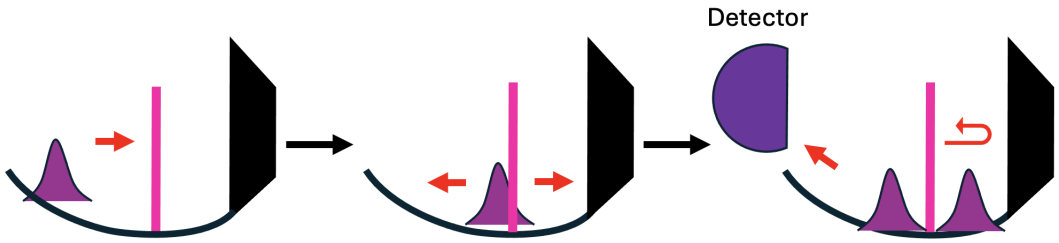

Fig. 2.8 Schematic Diagram for Generating Interference Patterns: The process begins with a single photon source producing a wavepacket. This wavepacket encounters a beam splitter, creating both a reflected and a transmitted wavepacket. Upon reaching a hard wall, the transmitted photon undergoes reflection, interfering with the previously reflected photon. A detector is located on the left to record the interference. It is worth noting that the distance between the wall and the beam splitter is usually greater than the width of the wavepacket, falling within the "sub-Rayleigh" regime. Additionally, this discussion focuses solely on the first-order process, disregarding any subsequent splitting after the initial encounter with the beam splitter.

measured by the receiver,

$$|\psi_c\rangle = \frac{q}{\sqrt{n}}|\psi_+\rangle + \frac{1-q}{\sqrt{n}}|\psi_-\rangle, \quad \text{where} \quad |\psi_\pm\rangle \triangleq \int_{-\infty}^{\infty} \mathrm{dx}\,\psi\left(\mathrm{x} - \mathrm{l}_0 \pm \frac{1}{2}\right)|\mathrm{x}\rangle. \tag{2.23}$$

Here, l_0 is the unknown centroid, n the normalization factor and q is the normalized intensity, defined as the ratio of N_+, the intensity of the first reflected photon, to N_{total}, the total intensity. The main difference between this model and the Star-Exoplanet model is that my quantum state is pure or coherent. For pure state, the Quantum Fisher Information Matrix $\mathscr{Q}$ is [15]:

$$\mathscr{Q}_{ij} = 4\mathrm{Re}[\langle\partial_i\psi|\partial_j\psi\rangle^2 - \langle\partial_i\psi|\psi\rangle\langle\psi|\partial_j\psi\rangle]. \tag{2.24}$$

By incorporating Eqn.(2.23), it becomes apparent that components $|\partial_l\psi_c\rangle$, $|\partial_q\psi_c\rangle$, and $|\partial_{l_0}\psi_c\rangle$ are essential for the three-parameter estimation problem. The simplest one to compute is the intensity derivative:

$$|\partial_q\psi_c\rangle = \partial_q\left(\frac{q}{\sqrt{n}}\right)|\psi_+\rangle + \partial_q\left(\frac{1-q}{\sqrt{n}}\right)|\psi_-\rangle. \tag{2.25}$$

For the remaining two, I can employ the technique introduced in Ref.[26]:

$$|\psi_\pm\rangle = \exp[-i(l_0 \mp l/2)P]\,|\psi\rangle, \tag{2.26}$$

where P represents the momentum operator $P = -i\partial_x$, responsible for generating displacements in the x variable. The expression for the derivative regarding centroid displacement can be formulated as follows:

$$|\partial_s \psi_c\rangle = \partial_l \left(\frac{q}{\sqrt{n}}\right)|\psi_+\rangle + \partial_l \left(\frac{1-q}{\sqrt{n}}\right)|\psi_-\rangle + \frac{q}{\sqrt{n}}|\partial_l \psi_+\rangle + \frac{1-q}{\sqrt{n}}|\partial_l \psi_-\rangle \tag{2.27}$$

$$= \hat{A}|\psi_+\rangle + \hat{B}|\psi_-\rangle \tag{2.28}$$

where $\hat{A} = -\frac{q\partial_l n}{2n^{3/2}} + \frac{q}{\sqrt{n}}(\frac{iP}{2})$ and $\hat{B} = -\frac{(1-q)\partial_l n}{2n^{3/2}} + \frac{1-q}{\sqrt{n}}(\frac{-iP}{2})$.

Similarly, the derivative concerning centroid position yields:

$$\left|\partial_{l_0}\psi_c\right\rangle = \frac{q}{\sqrt{n}}(iP)|\psi_+\rangle + \frac{1-q}{\sqrt{n}}(iP)|\psi_-\rangle\,. \tag{2.29}$$

Finally deriving the integral identities, $\langle\psi_\pm|P^2|\psi_\pm\rangle = \frac{1}{4\sigma^2}$ and $\langle\psi_\pm|P^4|\psi_\pm\rangle = \frac{3}{256\sigma^6}$ simplifies the calculation of Quantum Fisher Information significantly.

2.2.2 Main Results

We aim to assess the precision of my quantum parameter estimation against classical methods. Typically, it is advantageous to quantify precision as $H_\theta^{\text{opt/dd}} = 1/\text{Var}^{\text{opt/dd}}(\hat{\theta})$ for the unknown parameter θ. The superscript "opt" and "dd" denote the optimal quantum method and the classical direct detection approach. To initiate this comparison, let us outline the advancements and enhancements observed in quantum optimal measurement in contrast to classical approaches:

1. When the reflected source is weak due to loss, as q tends to 0 or 1, H_l^{opt} tends towards zero. The limit suggests that discerning between two vastly different wavepackets becomes challenging, if not impossible, especially when one pulse dominates detection. However, we anticipate a non-zero Quantum Fisher Information for normalized intensity estimation as q approaches 0 or 1, denoted by $\lim_{q\to 0,1} H_q^{\text{opt}} \neq 0$, since we know that the intensity of one wavepacket is either one or zero. Indeed, the scaling for brightness estimation is $\lim_{q\to 0,1} H_q^{\text{opt}} \sim l^2$.

2. For small separations, we expand l to higher orders:

$$H_l^{\text{opt}}(q,l) \sim \left(q^2 - 2q^3 + q^4\right) l^2 + O\left(l^4\right), \tag{2.30}$$

$$H_q^{\text{opt}}(q,l) \sim l^2 + \left(\frac{-1+4q-4q^2}{8}\right) l^4 + O\left(l^5\right). \tag{2.31}$$

At tiny separations, H_l^{opt} consistently tends towards zero, demonstrating the inevitability of the Rayleigh curse in this scenario. Notably, neither of the precision-bound functions depends on the centroid position l_0, as l_0 is integrated out in the Gaussian function. While obtaining the scaling relation for H_{l_0} is straightforward, this feature is less intriguing than the other two, and thus, I relegate it to Appendix B.1 for those interested.

3. In comparison, let us consider the expansion for direct detection:

$$H_l^{\text{dd}}(q,l) \sim \left(q^2 - 2q^3 + q^4\right) l^4 + O\left(l^5\right), \tag{2.32}$$

$$H_q^{\text{dd}}(q,l) \sim \frac{l^6}{384} + O\left(l^7\right). \tag{2.33}$$

Discovering the crossover point of the two methods by equating their expressions to 1 proves intriguing. However, achieving this analytically might pose challenges due to the presence of higher-order terms in both variables l and q. Instead, a more practical approach involves utilizing a heatmap to assess the quantum enhancements directly.

In Fig 2.9, the plot provides insights into the separation information H_l^{opt}, varying with both the separation l (in units of σ) and intensities q. Imbalanced intensities lead to a drop in precision, even at considerable separations. However, the right panel distinctly illustrates that the quantum method, characterized by the contour $H_l^{\text{opt}} = 0.05$, exhibits a broader distribution across intensity q, indicating its higher tolerance to intensity fluctuations.

A comparable examination is depicted in Fig 2.10, where the heatmap illustrates the precision of intensity ratio estimation. It is worth noting that precision remains intact for both methods even when there is a significant difference between the intensity coefficients of the two reflected wavepackets. Moreover, the quantum advantage is demonstrated by the finite precision value at small l/σ. Here, the optimal and classical information consistently demonstrate scaling behaviours of l^2 and l^6, respectively, with a noteworthy performance enhancement characterized by a l^4 gain.

Let us delve into the "sub-Rayleigh" region, where $l < \sigma$. The regime of significance in the log plots, as depicted in Fig 2.11, is readily discernible. Despite the marginal precision values for both techniques, the gap between optimal imaging and direct detection highlights the quantum advantages.

Analytically, for nearly balanced sources, $H_l^{\text{opt}} \propto l^2$ and $H_l^{\text{dd}} \propto l^4$. For unbalanced sources, if q approaches zero, then $H_l^{\text{opt}} \propto q^2 l^2$, and $H_l^{\text{dd}} \propto q^2 l^4$. Consequently, there is consistently a l^2 improvement factor with optimal detection compared to the standard method, regardless of the signal parameters. In practical terms, this implies that when we are below the Rayleigh

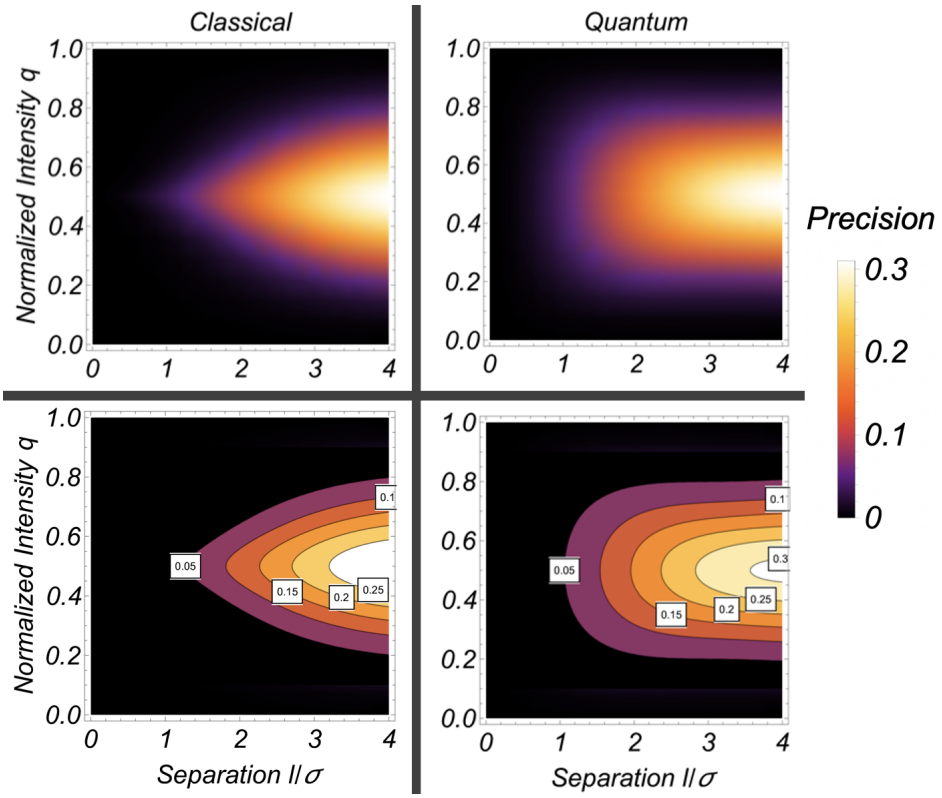

Fig. 2.9 Precision H_l depicted in a heatmap. In the top row, the absence of contour lines is notable. Darker regions signify significant difficulty in resolving the range distance, while brighter areas indicate a capacity to estimate l with some degree of accuracy. The colour bar on the right delineates the precise values of precision. Contour lines are now incorporated into the bottom row, with white labels denoting the precision values. The advantage of the optimal (quantum) method on the right over its classical counterpart on the left is evident in the rounded distribution of isolines, ensuring sustained precision in estimating parameter l. Direct imaging exhibits only a sharp peak, rendering estimation challenging in scenarios with unequal intensity coefficients.

limit, reducing the separation by a factor of 10 necessitates detecting approximately 10,000 times more photons using a CCD camera to maintain measurement accuracy. However, for optimal measurement, only 100 times more photons would be necessary, resulting in a 99% reduction in detection time with the optimal detection scheme.

The enhancements in intensity estimation precision also become apparent when inspecting the logarithmic plot, where a noticeable gap emerges between optimal measurement and the classical method. Interestingly, the variation in intensity difference does not significantly affect the separation estimation, as evidenced by the overlapping curves plotted.

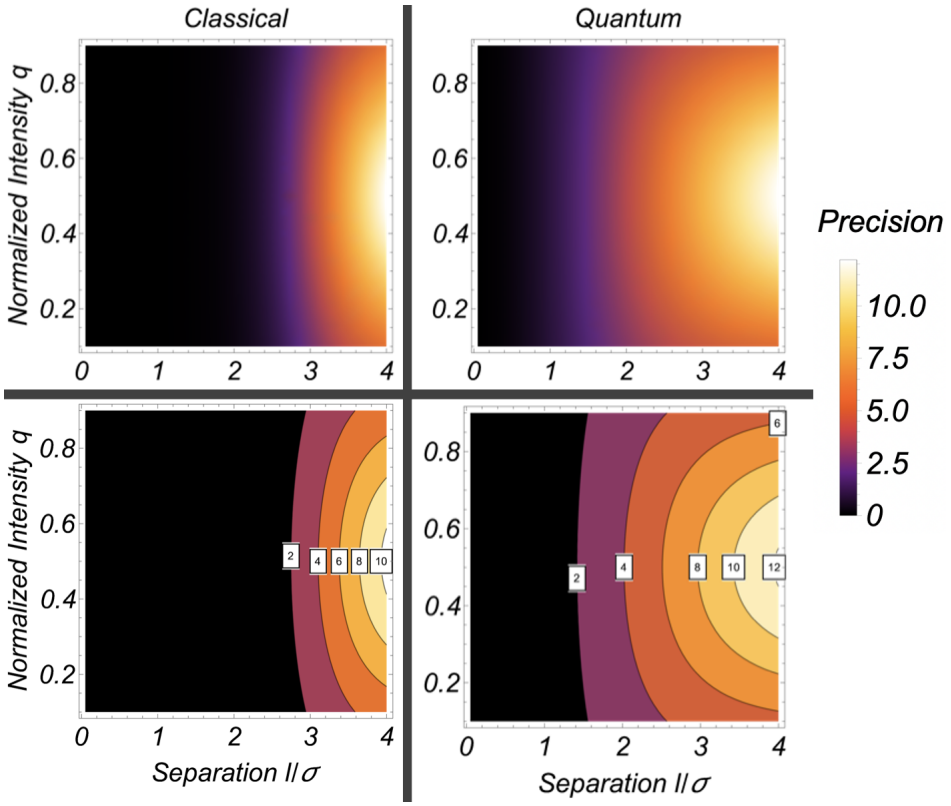

Fig. 2.10 The heatmap displays H_q^{opt} on the right column and H_q^{dd} on the left column. Isolines corresponding to a precision value of 2 are observed at approximately $l/\sigma \sim 1.5$ and $l/\sigma \sim 3$ for quantum and classical methods, respectively, highlighting the quantum advantage. It is worth noting that the precision values are generally higher than those for separation estimation.

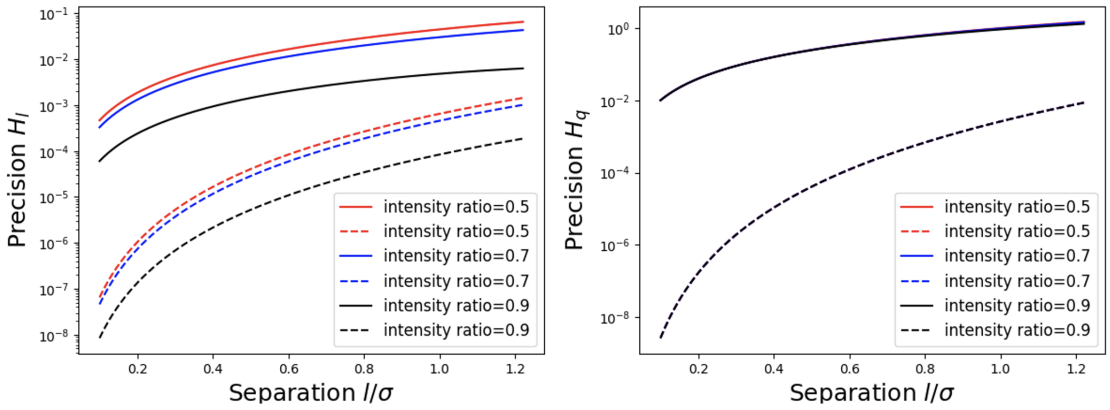

Fig. 2.11 Precision plots in logarithmic scale against l/σ are depicted. On the left, precision H_l^{dd} (represented by dotted lines) and H_l^{opt} (represented by solid lines) for direct detection and optimal detection, respectively, are illustrated. Three different intensities of the two sources are plotted and labelled on the side as 0.5 (balanced), 0.7, and 0.9. It is worth noting that due to the symmetry of q about 0.5, only $q \geq 0.5$ is considered. The gap between the dotted and dashed lines indicates a higher precision for the quantum method. While precision for separation estimation decreases with increasingly unbalanced intensities, the precision for intensity estimation remains almost independent of q, as evident from the overlap on the right.

Chapter 3

Final remark

This thesis presents the fundamental quantum limits for localizing incoherent sources and utilizing coherent sources to investigate "sub-Rayleigh" features.

For incoherent estimation, I provide an intuitive explanation of the quantum limit in scenarios characterized by high intensity contrast. The improvement of estimation over conventional methods is accomplished by employing hypothesis testing. I demonstrate that the quantum counterpart of hypothesis testing yields a quadratic improvement in relative entropy, naturally resulting in a reduction in type-II error. By progressively refining estimation and optimizing the POVM, my algorithm aims to attain the best estimate. Due to challenges associated with performing mode decomposition in the lab, quantum methods like SPADE are less practical than my proposal, which only necessitates measurements in the position basis and some optical transformations. However, the question that remains to be answered is whether there are significant improvements in the final estimate over classical methods rather than just a boost in type-II error. The intensity imbalance between the two photon sources poses a challenge to SPADE methods. Further research incorporating the quantum filter proposed by Arvidsson [27] could aid in balancing the intensities between incoherent sources through post-selection.

Furthermore, I assess the robustness of quantum-optimal measurements in radar applications with coherent sources, evaluating their potential as viable technology theoretically and experimentally. Utilizing Quantum Fisher Information, my model showcases significant improvements over classical methods in estimating separation, centroid, and normalized intensity parameters. Precise intensity estimation is particularly crucial due to setup imperfections leading to energy loss in pulse sequences. Exploring the impact of altering pulse shapes could yield valuable insights into mitigating these challenges. Additionally, avenues such as incorporating entanglement appear promising as well [28].

References

[1] Carl W Helstrom. Quantum detection and estimation theory. *Journal of Statistical Physics*, 1:231–252, 1969.

[2] C Helstrom. Resolution of point sources of light as analyzed by quantum detection theory. *IEEE Transactions on Information Theory*, 19(4):389–398, 1973.

[3] Mankei Tsang. Resolving starlight: a quantum perspective. *Contemporary Physics*, 60(4):279–298, 2019.

[4] Mankei Tsang, Ranjith Nair, and Xiao-Ming Lu. Quantum theory of superresolution for two incoherent optical point sources. *Physical Review X*, 6(3):031033, 2016.

[5] Xiao-Jie Tan, Luo Qi, Lianwei Chen, Aaron J Danner, Pakorn Kanchanawong, and Mankei Tsang. Quantum-inspired superresolution for incoherent imaging. *Optica*, 10(9):1189–1194, 2023.

[6] et al. Howell, John C. Super interferometric range resolution. *Physical Review Letters*, 2023.

[7] Andrew N Jordan and John C Howell. Fundamental limits on subwavelength range resolution. *Physical Review Applied*, 20(6):064046, 2023.

[8] Yink Loong Len, Chandan Datta, Michał Parniak, and Konrad Banaszek. Resolution limits of spatial mode demultiplexing with noisy detection. *International Journal of Quantum Information*, 18(01):1941015, 2020.

[9] Manuel Gessner, Claude Fabre, and Nicolas Treps. Superresolution limits from measurement crosstalk. *Physical Review Letters*, 125(10):100501, 2020.

[10] Cosmo Lupo. Subwavelength quantum imaging with noisy detectors. *Physical Review A*, 101(2):022323, 2020.

[11] Zixin Huang and Cosmo Lupo. Quantum hypothesis testing for exoplanet detection. *Physical Review Letters*, 127(13):130502, 2021.

[12] W. A. Traub and B. R. Oppenheimer. *Direct Imaging of Exoplanets*, pages 111–156. Seager, S., 2010.

[13] Seth Lloyd. Enhanced sensitivity of photodetection via quantum illumination. *Science*, 321(5895):1463–1465, 2008.

[14] Kevin Liang, SA Wadood, and AN Vamivakas. Coherence effects on estimating general sub-rayleigh object distribution moments. *Physical Review A*, 104(2):022220, 2021.

[15] Jing Liu, Haidong Yuan, Xiao-Ming Lu, and Xiaoguang Wang. Quantum fisher information matrix and multiparameter estimation. *Journal of Physics A: Mathematical and Theoretical*, 53(2):023001, 2020.

[16] Fumio Hiai and Dénes Petz. The proper formula for relative entropy and its asymptotics in quantum probability. *Communications in mathematical physics*, 143:99–114, 1991.

[17] Tomohiro Ogawa and Hiroshi Nagaoka. Strong converse and stein's lemma in quantum hypothesis testing. *IEEE Transactions on Information Theory*, 46(7):2428–2433, 2000.

[18] Mark M Wilde. *Quantum information theory*. Cambridge university press, 2013.

[19] Luigi Santamaria, Fabrizio Sgobba, and Cosmo Lupo. Single-photon sub-rayleigh precision measurements of a pair of incoherent sources of unequal intensity. *Optica Quantum*, 2(1):46–56, 2024.

[20] Zhixian Yu and Sudhakar Prasad. Quantum limited superresolution of an incoherent source pair in three dimensions. *Physical review letters*, 121(18):180504, 2018.

[21] Ugo Zanforlin, Cosmo Lupo, Peter WR Connolly, Pieter Kok, Gerald S Buller, and Zixin Huang. Optical quantum super-resolution imaging and hypothesis testing. *Nature Communications*, 13(1):5373, 2022.

[22] Lov K Grover. A fast quantum mechanical algorithm for database search. In *Proceedings of the twenty-eighth annual ACM symposium on Theory of computing*, pages 212–219, 1996.

[23] A Trifonov and A Zavriyev. Secure communication with a heralded single-photon source. *Journal of Optics B: Quantum and Semiclassical Optics*, 7(12):S772, 2005.

[24] Matthew D Eisaman, Jingyun Fan, Alan Migdall, and Sergey V Polyakov. Invited review article: Single-photon sources and detectors. *Review of scientific instruments*, 82(7):071101, 2011.

[25] John C Howell, Andrew N Jordan, Barbara Šoda, and Achim Kempf. Super interferometric range resolution. *Physical Review Letters*, 131(5):053803, 2023.

[26] Jaroslav Řeháček, Z Hradil, D Koutnỳ, J Grover, A Krzic, and Luis Lorenzo Sánchez-Soto. Optimal measurements for quantum spatial superresolution. *Physical review A*, 98(1):012103, 2018.

[27] Joe H Jenne and David RM Arvidsson-Shukur. Unbounded and lossless compression of multiparameter quantum information. *Physical Review A*, 106(4):042404, 2022.

[28] Abdelali Sajia and Xiao-Feng Qian. Superresolution of two unbalanced point sources assisted by the entangled partner. *Physical Review Research*, 4(3):033244, 2022.

[29] Matteo GA Paris. Quantum estimation for quantum technology. *International Journal of Quantum Information*, 7(supp01):125–137, 2009.

Appendix A

Fisher Information

A.1 Details on Fisher Information

The main text details that Fisher Information pertains to the sensitivity towards parameter changes. Consequently, the score of a distribution, denoted as $\boldsymbol{S}$, inherently delineates the available information. Let X represent a random variable with a distribution of $p(\boldsymbol{x}|\boldsymbol{\theta})$, where $\boldsymbol{\theta}$ denotes specific unknown parameters of the distribution that I aim to estimate, and $\boldsymbol{x}$ generally denotes observed data. The score $\boldsymbol{S}$ of the distribution is a random vector defined as the gradient of the logarithm of the likelihood concerning the parameter,

$$\boldsymbol{S} = \nabla_{\boldsymbol{\theta}} \ln(p(\boldsymbol{x}|\boldsymbol{\theta})) = \frac{1}{p(\boldsymbol{x}|\boldsymbol{\theta})} \nabla_{\boldsymbol{\theta}} p(\boldsymbol{x}|\boldsymbol{\theta}). \tag{A.1}$$

The Classical Fisher information matrix $\mathscr{F}(\theta)$ is defined as the covariance of the score:

$$\mathscr{F}(\boldsymbol{\theta}) = \mathrm{Cov}[\boldsymbol{S}]. \tag{A.2}$$

Note that for single parameter estimation, this reduces the variance of the score. Explicitly, the entries in this matrix are given by:

$$\mathscr{F}(\boldsymbol{\theta})_{ij} = \int \frac{\partial_{\theta_i} \ln(p(\boldsymbol{x}|\boldsymbol{\theta})) \partial_{\theta_j} \ln(p(\boldsymbol{x}|\boldsymbol{\theta}))}{p(\boldsymbol{x}|\boldsymbol{\theta})} d\boldsymbol{x}. \tag{A.3}$$

The calculation of Quantum Fisher Information involves a more intricate derivation, which revolves around determining the optimal measurement set. The optimal measure is found by computing the Symmetric Logarithmic Derivative (SLD). Let's consider a density matrix $\hat{\rho}(\boldsymbol{\theta})$ parameterized by θ_μ. The SLD L_μ is defined as a Hermitian operator that satisfies the

Sylvester equation:

$$2\frac{\partial\hat{\rho}_{\boldsymbol{\theta}}}{\partial\theta_\mu} = L_\mu\hat{\rho}_{\boldsymbol{\theta}} + \hat{\rho}_{\boldsymbol{\theta}}L_\mu. \tag{A.4}$$

If we write the density matrix in the eigenbasis $\hat{\rho}(\boldsymbol{\theta}) = \sum_m \rho_m |\Psi_m\rangle\langle\Psi_m|$, the SLD operator explicitly following [29],

$$L_\mu = 2 \sum_{\substack{\alpha,\beta \\ \rho_\alpha+\rho_\beta\neq 0}} \frac{\langle\Psi_\alpha|\frac{\partial\hat{\rho}}{\partial\theta_\mu}|\Psi_\beta\rangle}{\rho_\alpha+\rho_\beta} |\Psi_\alpha\rangle\langle\Psi_\beta|. \tag{A.5}$$

And the Quantum Fisher Information Matrix is expressed as $\mathscr{Q}_{\mu\nu} = \mathrm{ReTr}(\hat{\rho}(\boldsymbol{\theta})L_\mu L_\nu)$.

A.2 Cramér-Rao lower bound

To simplify the derivation, I consider a single parameter estimation process. For notational simplicity, I omit the explicit variable dependence of $p(x|\theta)$ and denote it instead as just p. Moreover, ∂_θ will be used to denote $\frac{\partial}{\partial\theta}$. Let us first show that the score S is zero-mean.

$$\begin{aligned} E[S] &= \int p\cdot[\partial_\theta \ln(p)]\,dx \\ &= \int p\cdot\left[\frac{1}{p}\partial_\theta p\right]dx \\ &= \partial_\theta\int p\,dx \\ &= \partial_\theta(1) = 0. \end{aligned}$$

Using the zero-mean property of the score:

$$F(\theta) = Var[S] = E[S^2] = \int p\cdot[\partial_\theta \ln(p)]^2\,dx. \tag{A.6}$$

Now we consider the unbiased estimator $\hat{\theta}$, from which I get:

$$\partial_\theta\int(\hat{\theta}-\theta)p\,dx = 0,$$

$$-\int p dx + \int(\hat{\theta}-\theta)\partial_\theta p\,dx = 0,$$

$$\int(\hat{\theta}-\theta)\partial_\theta p\,dx = 1.$$

Writing the derivative as the logarithmic function, $\partial_\theta \ln p = \frac{1}{p}\partial_\theta p$, above expression becomes

$$\int (\hat{\theta} - \theta) p \partial_\theta \ln p \, dx = 1.$$

Squaring the integral and applying the Cauchy–Schwarz inequality, one obtains

$$\left(\int ((\hat{\theta} - \theta)\sqrt{p})(\sqrt{p}\partial_\theta \ln p) \, dx \right)^2 \leq (\int (\hat{\theta} - \theta)^2 p dx)(\int p[\partial_\theta \ln p]^2 dx). \tag{A.7}$$

The left-hand side squares to be one, and the first bracket on the right gives us the variance of the unbiased estimator, while the second bracket is the definition for Fisher Information. Therefore, I arrive at $\mathrm{Var}(\hat{\theta}) \geq \frac{1}{\mathrm{F}(\theta)}$ for a single measurement.

A.3 Advantage of SPADE and Partial coherent source

Assuming the Gaussian PSF, the q-th Hermite-Gauss (HG) mode in position basis is:

$$|\phi_q\rangle = \frac{1}{(2\pi\sigma^2)^{1/4}} \frac{1}{\sqrt{2^q q!}} \int dx H_q\left(\frac{x}{\sqrt{2}\sigma}\right) e^{-\frac{x^2}{4\sigma^2}} |x\rangle . \tag{A.8}$$

By simple integration and completing the square, I arrive at the

$$\langle \phi_q | \psi(x) \rangle = \frac{e^{-\frac{x^2}{8\sigma^2}}}{\sqrt{q!}} \left(\frac{x}{2\sigma}\right)^q, \tag{A.9}$$

where $\psi(x)$ is the PSF in the detection process. Defining $\alpha = \frac{x}{2\sigma}$ and substituting in the expansion coefficients I have:

$$|\psi(x)\rangle = e^{-\frac{1}{2}\alpha^2} \sum_{q=0}^{\infty} \frac{\alpha^q}{\sqrt{q!}} |\phi_q\rangle . \tag{A.10}$$

Consider a simple two-source model with Eqn.(1.8) and θ being the separation, the probability of detecting a photon in the q^{th} HG mode is given by the Poisson distribution:

$$p(q) = \frac{Q^q}{q!} e^{-Q}, \quad \text{where} \quad Q = \frac{\theta^2}{16\sigma^2}. \tag{A.11}$$

To get the Fisher Information, I begin by writing out explicitly,

$$\begin{aligned}\frac{d}{d\theta}(\ln p(q)) &= \frac{d}{d\theta}(-Q+q\ln(Q)-\ln(q!))\\ &= -Q'+\frac{q}{Q}Q'\\ &= (\frac{q}{Q}-1)\frac{2}{16\sigma^2}\theta\\ &= 2(q-Q)/\theta.\end{aligned} \tag{A.12}$$

Then from Eqn.(A.3):

$$\begin{aligned}\mathrm{F_{HG}} &= \sum_{q=0}^{\infty} p(q)\left[\frac{d}{d\theta}\ln(p(q))\right]\\ &= \sum_{q=0}^{\infty} p(q)\left[2(q-Q)/\theta\right]\\ &= \frac{4}{\theta^2}\mathrm{Var(q)}\\ &= \frac{1}{4\sigma^2}.\end{aligned} \tag{A.13}$$

The conventional imaging method gives the probability distribution of intensity in position basis:

$$\mathrm{P_{intensity}(x)} = \frac{1}{2}\frac{\mathrm{e}^{\frac{-1}{2\sigma^2}\left(\mathrm{x}-\frac{\theta}{2}\right)^2}+\mathrm{e}^{\frac{-1}{2\sigma^2}\left(\mathrm{x}+\frac{\theta}{2}\right)^2}}{(2\pi\sigma^2)^{\frac{1}{2}}}. \tag{A.14}$$

It is interesting to see what would happen if I were to add in some coherence characterized by μ, with the intensity being:

$$\mathrm{P^{\mu}_{intensity}(x)} = \frac{1}{2}\frac{\mathrm{e}^{\frac{-1}{\sigma^2}\left(\mathrm{x}-\frac{\theta}{2}\right)^2}+\mathrm{e}^{\frac{-1}{\sigma^2}\left(\mathrm{x}+\frac{\theta}{2}\right)^2}+2\mathrm{Re}(\mu)\mathrm{e}^{\frac{-1}{\sigma^2}\left(\mathrm{x}^2+\frac{\theta^2}{4}\right)}}{(2\pi\sigma^2)^{\frac{1}{2}}}. \tag{A.15}$$

Then we can see that in some regions, the Fisher information for direct imaging is greater than the quantum method as in the top of Fig A.1.

Finally, I used Maximal likelihood to differentiate the separation. We can see in the bottom of Fig A.1 that the error increases rapidly as the distance between the sources decreases.

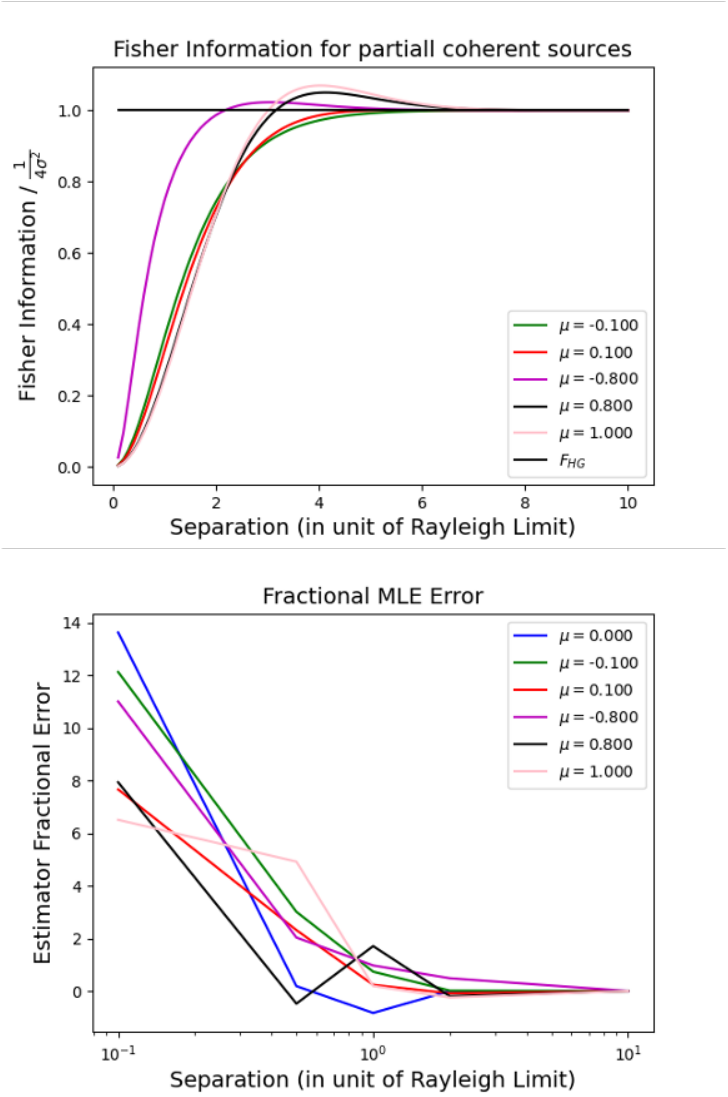

Fig. A.1 Top: Fisher information for imaging measurements for varying degrees (colors) of source coherence. The orange line shows the optimal quantum fisher information. Bottom: Calculated the Maximum Likelihood Estimator(MLE) $\hat{\theta}$ of the source separation for each of the simulated direct detection measurements ($N = 10^5$). The plot shows the fractional error $\frac{\hat{\theta}-\theta}{\theta}$ as a function of the source separation in a unit of σ for different coherence values.

Appendix B

Additional derivations

B.1 Analysis on Centroid estimation for Super Radar

Here, I conduct a similar analysis to that outlined in Sec. 2.2.2 regarding centroid-position estimation, focusing directly on the variance. The variances $\mathrm{Var}_{l_0}^{\mathrm{opt}}$ and $\mathrm{Var}_{l_0}^{\mathrm{dd}}$ for the optimal quantum method and classical direct detection are depicted in a heatmap (refer to Fig B.1).

Notably, the black region, indicating slight variance and precise estimation, appears to diminish from $l/\sigma = 4$ to $l/\sigma = 3$, only to revive when $l/\sigma < 2$, under similar intensity profiles. This revival directly demonstrates the superior efficacy of quantum imaging compared to the consistently high variance values observed in the small-separation region for the classical approach. Moreover, the overall variance scale is smaller by a factor of 3 for the quantum method. However, in severe energy loss (unequal intensities), neither method can precisely estimate the central position. Physically, according to my model, this implies that excessive energy loss hampers the ability to estimate the beam splitter's position accurately.

B.2 Derivation on Eqn.(2.16)

Let us further simplify the notation in Sec 2.1.2:

$$\psi_{star}(x - r_c) \to \psi, \tag{B.1}$$

$$\psi_{planet}(x - r_c - r_{est}) \to \hat{\psi}, \tag{B.2}$$

$$\psi_{planet}(x - r_c - r) \to \psi'. \tag{B.3}$$

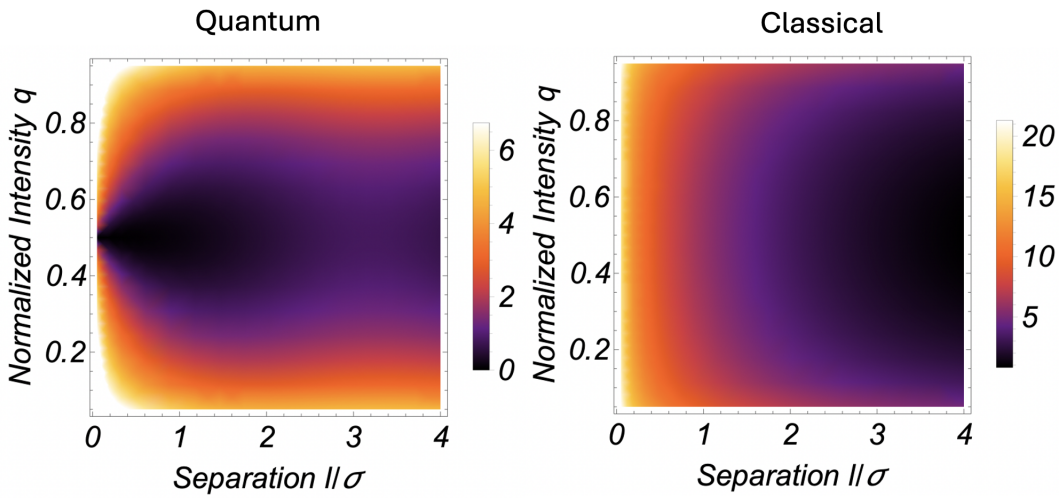

Fig. B.1 A heatmap illustrating the variance of the centroid (beam splitter) location estimation in the 'super radar' model. The symmetrical mirroring around $q = 0.5$ arises from the underlying system's symmetry. Darker colours indicate higher precision in parameter estimation, while lighter shades suggest lower precision during estimation. Notably, the quantum method exhibits lower variance on the left than classical imaging."

The full expression for the classical relative entropy for the two hypotheses is

$$\begin{aligned}
D(p_0\|p_1) &= \int dx p_0(x)\,[ln(p_0(x)) - ln(p_1(x))] \\
&= \int dx((1-\varepsilon)\psi^2 + \varepsilon\hat{\psi}^2)\left[ln\left((1-\varepsilon)\psi^2 + \varepsilon\hat{\psi}^2\right) - ln\left((1-\varepsilon)\psi^2 + \varepsilon\psi'^2\right)\right] \\
&= \int dx((1-\varepsilon)\psi^2 + \varepsilon\hat{\psi}^2)\left[ln\psi^2 + ln\left((1-\varepsilon) + \varepsilon\frac{\hat{\psi}^2}{\psi^2}\right) - ln\psi^2 - ln\left((1-\varepsilon) + \varepsilon\frac{\psi'^2}{\psi^2}\right)\right] \\
&= \int dx((1-\varepsilon)\psi^2 + \varepsilon\hat{\psi}^2)(\frac{\hat{\psi}^2}{\psi^2} - \frac{\psi'^2}{\psi^2})\left[\varepsilon - \frac{\varepsilon^2}{2}(\frac{\hat{\psi}^2}{\psi^2} + \frac{\psi'^2}{\psi^2} - 2)\right],
\end{aligned}$$

where in the last line, I have used the small expansion $ln(1+x) = x - \frac{x^2}{2}$ and regrouped similar terms. Typical terms like $\int dx\frac{\hat{\psi}^2}{\psi^2}$ can be evaluated by completing squares in the Gaussian integral, e.g.

$$\begin{aligned}
\frac{\hat{\psi}^2}{\psi^2} &= \frac{e^{-(x-r_c-r_{\text{est}})^2}/2}{e^{-(x-r_c)^2}/2} \\
&= e^{-r_{\text{est}}^2/2}e^{r_{\text{est}}(x-r_c)},
\end{aligned}$$

where the second part of the exponential introduces a shift in the Gaussian integral:

$$\begin{aligned}
&\int dx e^{-(x-r_c-r)^2/2} e^{r_{\text{est}}(x-r_c)} \\
&\quad = \int dx e^{-(x-r)^2/2} e^{r_{\text{est}}x} \\
&\quad = \int dx e^{-(x-(r_{\text{est}}+r))^2/2} e^{-(r_{\text{est}}+r)^2/2} e^{-r^2/2} \\
&\quad \sim e^{-r_{\text{est}}^2/2} e^{r_{\text{est}}r}.
\end{aligned}$$

Putting this all together and ignoring all higher order of ε, I finally have the expression for Eqn.(2.16).

Appendix C

Numerical results

C.1 Simulation

I have experimented with different intensity ratios by changing the transmitting coefficient of the beam splitter to compare the analytical results with the numerical ones as shown in Fig C.1. To dynamically simulate the evolution, I use the "Finite Difference Method" with time-dependent Shrödinger's equation (TDSE) in Python:

$$i\hbar\frac{\partial}{\partial t}\psi(x,t) = -\frac{\hbar^2}{2m}\frac{\partial^2}{\partial x^2}\psi(x,t) + V(x)\psi(x,t). \tag{C.1}$$

The goal of the Finite Difference Method is to take continuous derivatives, such as those found in Schrödinger's equation, $\frac{\partial}{\partial t}\psi(x,t)$ and $\frac{\partial^2}{\partial x^2}\psi(x,t)$, and transform them into discrete, computable functions.

To do this, let us go back to the fundamental definition of differentiation, with the definition of a derivative:

$$\frac{d}{dx}f(x) = \lim_{\Delta x\to 0}\frac{f(x+\Delta x) - f(x)}{\Delta x}, \tag{C.2}$$

where Δx is infinitesimally small. The issue lies in the limitation of performing this task on a computer. However, I can employ an approach involving exceedingly minute, finite steps to approximate the derivative. This method, known as the "Finite Difference Method", derives its name from this process.

Utilizing this method, I can ascertain the first-time derivative of the wave function, which appears on the left side of the Schrödinger's equation:

$$\frac{\partial}{\partial t}\psi(x,t) = \lim_{\Delta t\to 0}\frac{\psi(x,t+\Delta t) - \psi(x,t)}{\Delta t}. \tag{C.3}$$

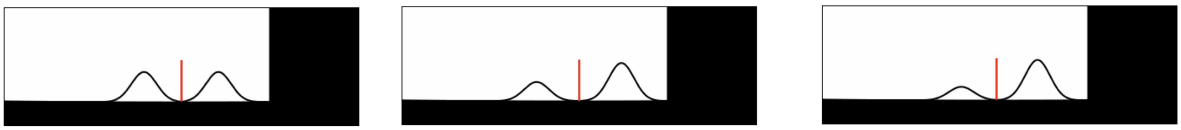

(a) Intensity ratio equals 1. (b) Intensity ratio equals 2. (c) Intensity ratio equals 3.

Fig. C.1 Three initial conditions for wavepacket evolution with a snapshot taken after the splitting and just before hitting the wall. Notice that the beam splitter (red) in the middle of two wavepackets is too small to see; thus, I have scaled it up for illustration. Moreover, the black space on the right has infinite potential corresponding to the wall.

Now, let us take the second spatial derivative present on the right-hand side of Schrödinger's equation. The first step is to find the first spatial derivative. Let us repeat the same process I did for the time derivative:

$$\frac{\partial}{\partial x}\psi(x,t) = \lim_{\Delta x \to 0} \frac{\psi(x+\Delta x,t) - \psi(x,t)}{\Delta x}. \tag{C.4}$$

In my animation, time progresses unidirectionally, displaying asymmetrical behaviour. Conversely, space in my animation spans two directions ($+x$ and $-x$). The derivative we have been employing thus far exhibits this asymmetry. To proceed, we will require a symmetric definition for the derivative:

$$\frac{d}{dx}f(x) = \lim_{\Delta x \to 0} \frac{f(x+\Delta x) - f(x-\Delta x)}{2\Delta x}. \tag{C.5}$$

Now, I can find the first spatial derivative of $\psi(x,t)$:

$$\psi'(x,t) = \frac{\partial}{\partial x}\psi(x,t) = \lim_{\Delta x \to 0} \frac{\psi(x+\Delta x,t) - \psi(x-\Delta x,t)}{2\Delta x}. \tag{C.6}$$

And the second derivative:

$$\begin{aligned}\frac{\partial^2}{\partial x^2}\psi(x,t) &= \frac{\partial}{\partial x}\psi'(x,t) = \lim_{\Delta x\to 0}\frac{\psi'(x+\Delta x,t)-\psi'(x-\Delta x,t)}{2\Delta x}\\ &= \lim_{\Delta x\to 0}\frac{\frac{\psi(x+2\Delta x,t)-\psi(x,t)}{2\Delta x} - \frac{\psi(x,t)-\psi(x-2\Delta x,t)}{2\Delta x}}{2\Delta x}\\ &= \lim_{\Delta x\to 0}\frac{\psi(x+2\Delta x,t)-2\psi(x,t)+\psi(x-2\Delta x,t)}{4\Delta x^2}\\ &= \lim_{\Delta x\to 0}\frac{\psi(x+\Delta x,t)-2\psi(x,t)+\psi(x-\Delta x,t)}{\Delta x^2}.\end{aligned}$$

I will drop the limits from here onwards to reflect that I use finite steps. I can now rewrite the Schrödinger's equation with my substitutes for the derivative:

$$\begin{aligned}&i\hbar\frac{\psi(x,t+\Delta t)-\psi(x,t)}{\Delta t}\\ &= -\frac{\hbar^2}{2m}\left(\frac{\psi(x+\Delta x,t)-2\psi(x,t)+\psi(x-\Delta x,t)}{\Delta x^2}\right)+V(x)\psi(x,t).\end{aligned}$$

And rearrange this formula, such that $\psi(x,t+\Delta t)$ is isolated:

$$\begin{aligned}\psi(x,t+\Delta t) &= \left(\frac{i}{2m}\right)\left(\frac{\Delta t}{\Delta x^2}\right)(\psi(x+\Delta x,t)-2\psi(x,t)+\psi(x-\Delta x,t))\\ &\quad -\left(\frac{i}{\hbar}\right)(\Delta t)V(x)\psi(x,t)+\psi(x,t)\end{aligned}$$

To make the updates more accurate, I used Runge–Kutta (RK) methods to the fourth order:

$$\begin{aligned}\psi(x,t+\Delta t) &= \psi(x,t)+\frac{\Delta t}{6}(k1+2*k2+2*k3+k4)\\ k1 &= \psi(x,t)\\ k2 &= \psi(x,t+\Delta t/2*k1)\\ k3 &= \psi(x,t+\Delta t/2*k2)\\ k4 &= \psi(x,t+\Delta t*k3)\end{aligned}$$

To numerically simulate a quantum system using the TDSE, I worked on a discrete grid of N_G (5000 equally-spaced points with spacing, Δx). To do this, I have to find a way to discretize the various components of the TDSE. The wave function at a point in time, $\psi(t)$,

and potential, V, can be discretized as vectors of length N_G in which each element contains the value of the wave function or the potential at the corresponding point on this grid. Discrete Laplace operator can be given as convolution with the kernel:

$$\begin{bmatrix} 1 & -2 & 1 \end{bmatrix},$$

which results in a symmetric tridiagonal Toeplitz matrix with the finite-difference coefficients along the diagonals. The discrete Laplace operator is then given by:

$$\nabla^{\mathbf{2}} = \frac{1}{\Delta x^2} \begin{bmatrix} -2 & 1 & & & \\ 1 & -2 & 1 & & \\ & & \ddots & & \\ & & 1 & -2 & 1 \\ & & & 1 & -2 \end{bmatrix},$$

where Δx is the spacing between points. If I have a potential, $\mathbf{V} = \begin{bmatrix} V_0 & V_1 & \dots & V_N \end{bmatrix}$, then the full Hamiltonian operator in matrix form is given by:

$$\hat{\mathbf{H}} = \frac{-\hbar^2}{2m\Delta x^2} \begin{bmatrix} -2 & 1 & & & & \\ 1 & -2 & 1 & & & \\ & & \ddots & & & \\ & & 1 & -2 & 1 & \\ & & & 1 & -2 & \end{bmatrix} + \begin{bmatrix} V_0 & & & & & \\ & V_1 & & & & \\ & & \ddots & & & \\ & & & V_{N-1} & & \\ & & & & V_N & \end{bmatrix}.$$

The potential is a harmonic well (stabilizing the Gaussian wavepacket from spreading) plus a delta function in the middle (beam splitter). Note: Because of the way I define the finite differences at the boundaries, the wave function will reflect ultimately at the boundaries. The edges of the simulation are effectively infinite-potential barriers.

The formula for the Gaussian pulse I used is:

$$\psi(x,0) \sim \left(e^{ip_0 x}\right) \left(e^{-\left(\frac{x-x_0}{2\sigma}\right)^2}\right), \tag{C.7}$$

where p_0 is the initial momentum of my wavepacket. One limitation of real computers is that numbers and operations are only sometimes precise, as computers are constrained by how much memory they can assign to any given number. So, the safest approach for normalization

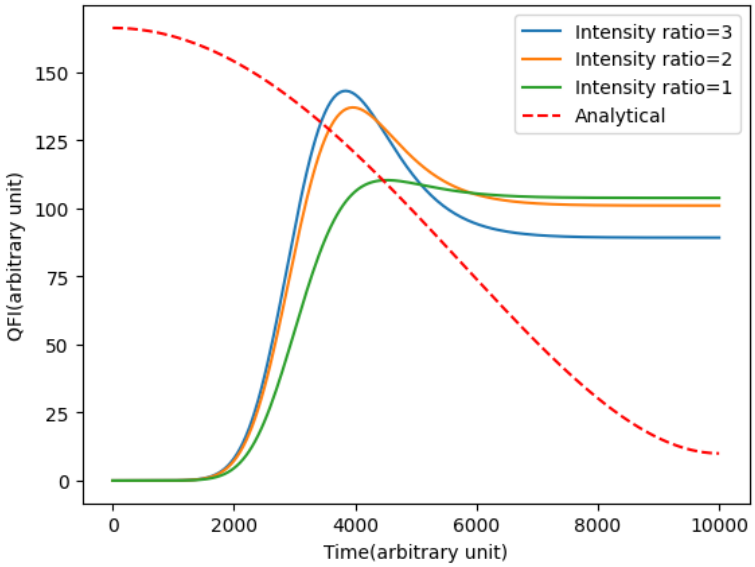

Fig. C.2 Time evolved Quantum Fisher Information (QFI) based on the Gaussian pulse for different initial intensity ratios of the forward and reflected wavepacket (controlled by the height of the beam splitter).

is to apply the following conditions:

$$\int_{-\infty}^{\infty} |\psi(x,t)|^2 \, dx = 1$$

directly in discretized space:

$$\sum |\psi(x,t)|^2 \, dx = 1.$$

As I recursively apply the normalization, numerical instability is prevented. The combined plot is shown in Fig C.2, where different solid lines indicate how the Quantum Fisher Information changes for pulses with various intensity differences with time. The dotted analytical line is plotted based on Eqn.(2.30) with scaling to fit the maximum Quantum Fisher Information obtained during the evolution.